

Landslide Analysis on Ceres

A Thesis
Presented to
The Academic Faculty

By

Heather Chilton

In Partial Fulfillment
of the Requirements for the Degree
Master of Science in the
School of Earth and Atmospheric Sciences

Georgia Institute of Technology
May, 2018

Copyright © Heather Chilton 2018

Landslide Analysis on Ceres

Approved by:

Dr. Britney E. Schmidt, Advisor
School of Earth and Atmospheric Sciences
Georgia Institute of Technology

Dr. Ken L. Ferrier
School of Earth and Atmospheric Sciences
Georgia Institute of Technology

Dr. James J. Wray
School of Earth and Atmospheric Sciences
Georgia Institute of Technology

Date Approved: April 27, 2018

ACKNOWLEDGEMENTS

I would like to sincerely thank my advisor Dr. Britney Schmidt, without whom none of this would have been possible and who has been my greatest advocate throughout this project. She opened the door for my graduate work, paved the way for this project, and offered endless support and constant motivation. I would also like to recognize the excellent suggestions and support offered by my committee members Drs Ken Ferrier and James Wray, who have helped strengthen this project into through their recommendations.

This project is also made possible by the hard work of the Dawn science and operations teams. The Dawn mission is managed by JPL for NASA's Science Mission Directorate in Washington and is part of NASA's Discovery Program out of Marshall Space Flight Center in Huntsville, Alabama. Spacecraft build is by Orbital ATK Inc, Dulles Virginia, and the specific instruments are part of international collaboration with the German Aerospace Center, Max Planck Institute for Solar System Research, Italian Space Agency, and Italian National Astrophysical Institute. Framing Camera data and Ceres' FC Global Mosaic can be accessed from NASA's Planetary Data System (PDS), and DTM listed in the references.

Finally I am incredibly grateful to my fiancée and two cats who tirelessly provided emotional support, even in the hardest of times. I am also grateful for the friends and family who have continually extended guidance and encouragement.

TABLE OF CONTENTS

ACKNOWLEDGEMENTS	iii
LIST OF TABLES	vi
LIST OF FIGURES	vii
LIST OF ABBREVIATIONS AND SYMBOLS	viii
SUMMARY	x
CHAPTER 1: INTRODCUTION	1
CHAPTER 2: LITERATURE REVIEW	6
2.1 Ceres Basics and Pre-Dawn.....	6
2.2 Ice at Ceres	7
2.3 Surface Composition	9
2.4 Landslides on Ceres.....	13
CHAPTER 3: METHODOLOGY	17
3.1 Data and Tools.....	17
3.2 Morphology and Categorization.....	18
3.3 Quantification and Measurements.....	20
3.3.1 <i>H/L</i>	20
3.3.2 <i>V-A</i> :.....	23
3.4 Ice Content Analysis.....	25
CHAPTER 4: RESULTS	27

4.1 <i>H/L</i> measurements	28
4.2 Volume-area measurements	30
4.3 Constraints on ice content using compositional constraints	33
CHAPTER 5: CONCLUSIONS	35
APPENDIX A: KEY DATA	41
REFERENCES	46

LIST OF TABLES

Table 1	<i>H/L</i> value ranges Ceres and other planetary bodies	14
Table 2	FC image and DTM resolutions.....	17
Table 3	Relevant material friction coefficients.....	22
Table 4	<i>H/L</i> and V-A values for Cerean landslides.....	29
Table 5	Modeled compositions for Ceres' surface materials.....	32

LIST OF FIGURES

Figure 1	Ceres as seen during Dawn approach.....	3
Figure 2	Examples of T1 and T2 with counter examples	19
Figure 3	Latitudinal Distribution of Cerean Landslides	27
Figure 4	T1, T2, and IM <i>H/L</i> values compared with ranges for clays and ice	28
Figure 5	V-A of T1, T2, and IM landslides	31
Figure 6	Suggested subsurface structure and composition for Ceres as a function of latitude	39

LIST OF ABBREVIATIONS AND SYMBOLS

Abbreviation	Full Meaning
T1	Type 1 (Ceres landslide category)
T2	Type 2 (Ceres landslide category)
IM	Intermediate (Ceres landslide category)
VIR	Visible and Infrared Spectrometer (Dawn)
GRaND	Gamma Ray and Neutron Detector (Dawn)
FC	Framing Camera (Dawn)
WEH	Water equivalent hydrogen
Max	Maximum
CoM	Center of mass
IRTF	Infrared Telescope Facility
LDA	Lobate debris apron
LAMO	Low Orbit Mapping Orbit
HAMO	High Altitude Mapping Orbit

Symbol	Meaning
<i>H</i>	Height, elevation change of landslide
<i>L</i>	Length, travel distance of landslide
<i>m</i>	Mass
<i>g</i>	Gravity

R	Resistance coefficient
θ	Slope angle
F_{net}	Net force
μ	coefficient of friction
H_{Max}/L_{Max}	Apparent coefficient of friction using maximum H and maximum L
H_{CoM}/L_{CoM}	Apparent coefficient of friction using CoM H and CoM L
V	Volume of landslide scar
A	Plan-view area of landslide scar
α	Volume-Area intercept
γ	Volume-Area scaling exponent

SUMMARY

I analyze landslides on Ceres using several quantitative approaches to constrain the composition and structure of the top few kilometers of Ceres' crust. I focus on a subset of archetypal landslides classified morphologically as thick, steep-snouted "type 1" (T1) flows and thin spatulate "type 2" (T2) flows (Schmidt et al., 2017) to explore the landslides' mechanical properties, and supplement with comparison with all landslides combined. The results confirm earlier observations showing that T1 landslides are typically found poleward of 70° latitude and T2 mostly equatorward of 70° latitude. Measurements of landslide drop height and runout length imply effective friction coefficients lower than common friction coefficients in any of Ceres' identified or suggested non-ice surface materials, including saturated clays. Measurements of the volume and area of landslide scars suggest that T1 landslides can fail to greater depths than T2 specifically and most landslides overall for a given scar area, consistent with depth-limited failure in landslides below 70° latitude. These results are consistent with a layer of lower shear strength material overlying a stronger layer in Ceres' outer shell at low to mid latitudes, and a single layer without an overlying weak layer at polar latitudes. Combining these observations with known constraints on Ceres' near-surface composition, I propose that Ceres' crust at low to mid latitudes consists of a topmost layer with an ice content in excess of the near surface that thins out at high latitudes, and which overlies a somewhat stronger and more ice-rich layer.

CHAPTER 1: INTRODCUTION

Landslides occur throughout the solar system, from icy satellites such as Iapetus (Singer et al., 2012) and Callisto (Chuang and Greeley, 2000) to dwarf-planet Ceres (Buczkowski et al., 2016; Schmidt et al., 2017) to Mars' Valles Marineris (Lucchitta, 1979; McEwen, 1989; Watkins et al., 2015). The ability of a landslide to move depends on its initial failure, kinetic energy, internal properties, and interaction with the surfaces over which it moves. Landslides on planetary surfaces outside of the Earth have been partially analyzed in terms of their apparent, or effective, coefficient of friction and its inverse, referred to as the flow efficiency (Iverson, 1997) or (velocity-independent) mobility (Iverson et al., 2015; Legros, 2002; Singer et al., 2012). Long runout landslides, generally defined as those where the materials in a landslide deposit travels farther than would be predicted by simple friction models applied to common rocks types, are among the most prevalent. A reduction in friction during landsliding can occur via an extensive range of mechanisms and have been summarized in multiple works (Voight, et al., 1983; Legros, 2002; De Blasio, 2011) but in brief include fluidization from air (Kent, 1966; Shreve, 1966, 1968; Fahnstock, 1978), suspension by particle distributions or vibrations (Hsü, 1975; Melosh, 1979), and an increased mobility by warmed ice or liquid water (Legros, 2002; Singer et al., 2012; Erismann & Abele, 2013; De Blasio, 2014). The latter is commonly invoked for landslides on other planets (Lucchitta, 1979; De Blasio, 2011; Singer et al., 2012).

Ceres (Figure 1), located in the main asteroid belt, provides a unique look at planetary landslides and related landforms for a number of reasons. First, the Dawn spacecraft at the time of this writing is currently orbiting the body, providing new data on a previously

poorly characterized body. As such, a geomorphic analysis of the features is important to help understand the materials and processes at work on the surface of Ceres. Second, Dawn's dedicated orbit around Ceres provides some of the best and consistently high-resolution coverage of a body in the solar system other than Earth and Mars, particularly compared with the satellites of the outer solar system. This allows us to conduct a global study and accurately evaluate and compare the landslides and related features. Third, the surface is old and relatively unaffected by processes other than impact cratering and mass wasting, establishing a global study that isolates near-surface material properties as one of the few variables involved – at least compared with the geographically variable and much more processed surfaces of Earth and Mars. Finally, recent work has shown a latitudinal dependence of lobate flows may be indicative of increased H₂O ice content and viscosity – due to decreased temperatures – towards the poles (Schmidt et al., 2017). That Ceres possesses an ice-silicate composition offers a unique point of contrast to other planetary bodies.

Features mapped as landslides on Ceres are found both interior and exterior to impact crater rims (Buczkowski et al., 2016; Schmidt et al., 2017). Schmidt et al. (2017) identified three main categories of surface flows exclusionary of impact-induced crater floor mass wasting flows, two of which are consistent with landslides and are categorized as Type 1 (T1) and Type 2 (T2) (Figure 2). Type 3 flows have been interpreted as processes related to ejecta, rather than landslides (Schmidt et al., 2017; Hughson et al., in review). Those features were classified based on morphology, with T1 landslides characterized as thick, lobate, and steep snouted and initiating on steep slopes. T2

landslides, by contrast, were identified as thin, long-runout flows, capable of motion across moderate to shallow slopes.

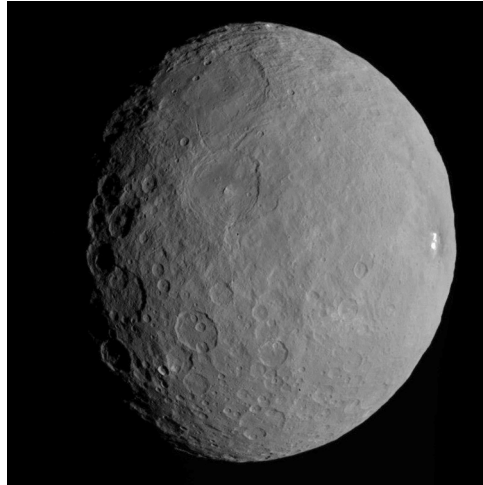


Figure 1: Ceres, seen during Dawn approach

Landslides on Ceres have been interpreted as evidence of ground-ice (Buczowski et al., 2016; Schmidt et al., 2017). Thermal calculations define the boundary to the ice table as the depth at which ice loss is less than 1 meter per Gyr (Hayne and Aharonson, 2015; Landis et al., 2017). Along with analysis of neutron spectroscopy data, studies have placed this boundary at 10 - 100 meters depth at the equator, with more recent work suggesting depths of closer to 1 meter, to possibly exposed at the surface of the poles (McCord and Sotin, 2005; Hayne and Aharonson, 2015; Platz et al., 2016; Schorghofer, 2016; Landis et al., 2017; Prettyman et al., 2017).

However, the amount and distribution of ice below a few meters depth, and interaction of this ice with other materials, are comparatively less well understood. Further, the ice table boundary is commonly calculated as the depth at which ice is stable for billions of

years (Hayne and Aharonson, 2015), but this reflects a stability boundary and may not reflect the actual ice-bearing boundary, which could be affected by impact stirring and other processes (Schorghofer, 2016), or any transition into layers with higher ice content. Here we present new measurements of landslides mapped using imagery and topographic data from the Dawn Framing Camera to expand our understanding of Ceres surface geology and its implications for subsurface structure.

Previous analyses showed that T1 and T2 landslides differ in geographic location and mobility. Schmidt et al., (2017) found that T1 flows occur predominately in polar latitudes, and used measurements of the landslides' drop height (H) and runout length (L) to show that T1 flows typically have height H/L values – and hence a lower mobility – than T2 flows, which occur predominately in low to mid latitudes. Schmidt et al. (2017) concluded that the distribution and morphology of the flow deposits implied the presence of subsurface ice, and that T1 flows indicated higher ice content than T2 flows.

These interpretations agree well with other observations by the Dawn spacecraft that suggest the presence of significant ice: Ceres' outer 190 kilometers has a density of 1,680 – 1,950 kg/m³ (Park et al., 2016), consistent with pre-Dawn estimates of 16% – 27% ice by mass (McCord and Sotin, 2005; Thomas et al., 2005); crater morphologies indicate an outer shell tens of km thick and comprised of 30 - 40% ice, although plausibly higher if clathrates – ice structural “cages” around, in this case, likely methane – are included (Bland et al., 2016); spectral detections by Dawn's Visible and Infrared Spectrometer (VIR) indicate at least nine locations with exposed ice including at Juling crater (Combe et al., 2016; Combe et al., 2017; Formisano et al., 2017; Raponi et al., 2017); and water equivalent hydrogen (WEH) determined by the Gamma Ray and Neutron Detector

(GRaND) suggests that the upper few decimeters to meter of regolith could contain as much as 15% ice by volume at the equator and up to 30% ice at the poles (Prettyman et al., 2017), although their estimates subtract the polar from the equatorial values to establish ice content due to ice stability depths deeper than detection depths.

Exposed ice is unstable over most of Ceres' surface, as indicated by the thermal stability depths described previously, suggesting detected exposures of ice are recent and that ice content below the surface exceeds spectrally derived compositions. This is reflected in the GRaND WEH data. Prettyman et al (2017) suggest there is an ice table comprised of 10% water ice by taking the ice table as within a few centimeters of the polar surface and subtracting the equatorial hydrogen from polar measurements. However, because GRaND can detect hydrogen to no more than ~1 meter in depth, it does not reveal how much ice may lie deeper below the surface. The identification of surface materials and properties such as frictional behavior or strength can help constrain landslide behavior, which in turn can help constrain ice concentrations at greater depths than GRaND.

In order to constrain the character of Ceres' surface materials beyond the top >1 meter sampled by GRaND and spectrometers, we expand previous work on the Cerean landslides. Here, we present new measurements of Cerean landslide mobility and failure geometries, and apply constraints from literature to refine our interpretations of the structure and ice content of the top few kilometers of the Cerean subsurface.

CHAPTER 2: LITERATURE REVIEW

2.1 Ceres Basics and Pre-Dawn

Ceres is a dwarf-planet in the main asteroid belt and contains nearly a third of the entire mass of the belt. Pre-Dawn work on Ceres roughly determined its density and surface properties, modeled its internal structure, and constrained surface temperatures, all indicating that Ceres is an ice-silicate mixture (McCord and Sotin, 2005; Russell and Raymond, 2011). The intriguing possibility of Ceres containing substantial H₂O paired with the potential to provide insight into early solar system planetary formation identified Ceres as a prime target for further study, motivating the Dawn mission (Russell and Raymond, 2011). In 2007, the Dawn spacecraft launched, aiming to elucidate early solar system evolution by visiting dry, rocky Vesta and ice-silicate Ceres, both believed to have been prematurely aborted from full planetary growth by Jupiter (Thomas et al., 2005). The spacecraft carries with it three types of instruments: the two Framing Cameras (FC), the VIR, and GRaND. In addition, tracking of the motion of the spacecraft using its onboard radio antennas provides constraints on the gravity and internal structure of Ceres. In March 2015, Dawn entered Ceres orbit.

Both Vesta and Ceres, with average radii of 263 km and 473 km respectively, are believed to have been prematurely aborted from full planetary growth by the massive gravity well of Jupiter depleting material from the region, thus preserving a surface record of this early evolution (Thomas et al., 2005). Ceres in particular provides a window into the behavior and characteristics of a body in a transition region between the solar systems rocky and icy worlds: With an orbit ranging from 2.56 AU out to 2.98 AU,

Ceres crosses the so-called “ice-line” or “snow-line,” an approximate boundary currently between 2.7 – 3.2 AU (Dodson-Robinson, et al., 2009; Hayashi, 1981; Martin & Livio, 2013) beyond which water will freeze instead of remaining a vapor. Supporting the conclusion of Ceres as an ice-silicate mixture and consistent with formation near this ice-line, Ceres’s average density is 2161 kg/m^3 (Park et al., 2015) resulting in an estimated ice by volume of ~25% (Russell et al., 2015). Comparatively, Vesta has a density of $\sim 3460 \text{ kg/m}^3$ (Russell and Raymond, 2011), making it significantly more rocky than Ceres. Further, while Vesta is considered to be a fully differentiated body, the degree of differentiation for Ceres is currently being revisited: current work estimates Ceres to be weakly differentiated and eroded from sublimation and bombardment (Castillo-Rogez et al., 2016). Ceres is, however, likely comprised of a rocky core with an ice-silicate outer mantle and surface silicate lag deposit, although degree of mixture, depths, and additional components are debated (McCord & Sotin, 2005; Thomas et al., 2005; Raymond et al., 2015; Schenk et al., 2015).

2.2 Ice at Ceres

At Ceres’ surface, temperature controls the presence of exposed ice or, where unstable at the surface, the depth to ice stability; this directly impacts detection by instruments such as Dawn’s GRaND and VIR instruments, which measure composition of the surface. With no atmosphere, surface temperatures range from 243 K at the equator to 119 K at the poles (Hayne and Aharonson, 2015), making surface ice unstable – instead, it will sublimate away and leave behind a silicate surface lag layer. However, given ~1 meter of porous insulating material, comparable to this lag deposit, ice can persist for

more than a billion years above 50° latitude (Hayne and Aharonson, 2015), suggesting that even a modestly thick surface lag layer will retain subsurface ice at low latitudes. Despite the instability of ice at the surface, events exposing a fresh surface could reveal such ice from the subsurface until fully sublimated: Hydroxyl was reported above localized areas of Ceres, suggesting water vapor (Küppers et al., 2014) from either surface sublimation or endogenic sources. GRaND results indicate increased hydrogen content towards the poles, but does not distinguish between water-ice and OH⁻ or H₂O-bearing minerals (Prettyman et al., 2016) while the VIR indicates ammoniated phyllosilicates (De Sanctis et al., 2016) and H₂O, either from ice or mineral hydrates (Combe et al., 2016).

Ice content in the upper layer of Ceres has been a dynamic discussion with the recent wave of data from Dawn. Two primary works, both involving impact craters, address the outer tens of kilometers of Ceres. Impact craters, which relax and flatten at rates that depend on regolith strength, indicate that the top 25 – 40 km of Ceres contains less ice than expected and should not be predominantly ice; instead, Ceres should consist of less than 40% ice relative to silicates, be significantly rich in salts, or some combination thereof (Bland et al., 2016). In contrast, the diameter at which craters transition from the smooth, bowl-like simple craters into complex craters is a function of surface gravity and impacted surface material: plotting this transition diameter versus surface gravity provides distinct lines for icy and rocky bodies, and Ceres closely aligns with the icy-satellites line, suggesting an ice-rich layer broadly constrained to tens of kilometers thick (Schenk et al., 2015).

2.3 Surface Composition

The best constraints on the mineral composition of Ceres' surface materials are derived from spectral data from the VIR instrument (De Sanctis et al., 2015; Ammannito et al., 2016) and earlier work using the NASA Infrared Telescope Facility (IRTF) (Lebofsky, et al., 1981; Rivkin, Volquardsen, & Clark, 2006). Down to the spectral sampling depth of a few millimeters, Ceres' surface is predominantly comprised of a spectrally neutral material intermixed with lesser amounts of OH⁻, Fe⁻ and Mg⁻ phyllosilicates that may contain NH₄⁻, as well as carbonates and other selected minerals that vary between authors. More recent VIR observations, limited to below 60° latitude, suggest a largely spatially homogeneous composition with heterogeneous abundances of Mg- and NH₄-phyllosilicates from 6-12% and 3-9% respectively (Ammannito et al., 2016). The phyllosilicates are typically interpreted as clays, of which the most commonly invoked are montmorillonite, cronstedtite, and antigorite or tochilinite (Rivkin et al., 2006; Ammannito et al., 2016; De Sanctis et al., 2015). VIR results in the ~2.5-2.9 μm range, which were not possible in Earth-based observations, suggest intermixed Mg-phyllosilicates or tochilinite with Fe-phyllosilicates, carbonate, magnetite, and possible ammoniation due to the observed 3.05 – 3.1 μm band at Ceres (De Sanctis et al., 2015). Ammoniation is preferred by De Sanctis (2015), and is argued as evidence for an outer solar system origin for Ceres. Rivkin et al. (2006) prefer Fe-rich phyllosilicates to ammoniation due to a spectral feature in the mid-infrared.

Spectral detection limits may inform about minimum abundances, particularly for low abundance estimates: at least 10% clay is necessary for detection in a salt Mg-sulfate epsomite mixture (Stack and Milliken, 2015), supporting a lower bound for

phyllosilicates; carbonate content was accurately determined to within 1-2 wt% in a terrestrially based study, even at low abundances, in the IR spectral range (Kaufhold et al., 2012). Carbonates, typically only found on Earth and Mars, could have formed from aqueous alteration and both dolomite and cronstedtite produced the best modeled spectral fits (Rivkin et al., 2006). The composition of the spectrally neutral material cannot be directly addressed by our landslide observations, but we note that the addition of weak materials would reduce bulk material strength (Kozłowski & Nartowska, 2013, and references therein) and affect the friction coefficient, especially in the case of the very weak montmorillonite (Morrow, Radney, & Byerlee, 1992; Saffer, et al., 2001; Tembe, Lockner, & Wong, 2010).

Aside from melting during impacts, Ceres' surface has been uniformly exposed to the vacuum of space over the lifetime of the solar system, and has likely spent the majority of this time near its current position in the asteroid belt, such that rates of mineral alteration have likely been slow for most of this time. Moreover, Dawn results indicate that Ceres has undergone relatively little differentiation (Fu et al., 2017), producing a composition that should mirror alteration of an original chondritic or mafic composition. Early aqueous alteration may have been extensive, as indicated by Ceres' relatively low density (Park et al., 2016; Bland & Travis, 2017), providing an abundance of water to form hydrated clay assemblages. This presents an avenue for early formation of clays on Ceres, while the upper few kilometers should undergo continual, if irregular, alteration through impact heating that, outside the boundary where vaporization occurs, could both melt ice or liberate bound water from minerals.

One phyllosilicate to consider is the serpentine cronstedtite, an early product of aqueous alteration in carbonaceous chondrites (Dyl et al., 2012; Rubin, 2012) and found in analyses of carbonaceous chondrites (Bass, 1971; Barber, 1981); however with continued alteration it would progress into Mg-rich serpentines, saponite, and vermiculate (Castillo-Rogez and Young, 2017). Smectites, notably montmorillonite, have also been an identified or suggested component in carbonaceous chondrite compositional analyses (Bass, 1971; Johnson & Fanale, 1973; Barber, 1981; Tomeoka & Buseck, 1982).

Due to the presence of either OH or H₂O, or combinations thereof, into a layered structure, clays are considered hydrated phyllosilicates. Common examples include kaolinite, the serpentine lizardite, and the smectite montmorillonite. Most clays are classified based upon layering structure, all containing OH, but only some containing H₂O. A special class of clays is identified by its swelling capacity, called smectites, and overlap with different layering classes of other clays; these have both OH and varying amounts of water, denoted $n\text{H}_2\text{O}$ and up to $n = 10$, within their structure. This last provides for the possibility of significant inclusion of water within the clay by montmorillonite.

Freezing of water-bearing clays can result in ice lensing and the development of cracks within the material, which grow extensive even after only one freeze-thaw cycle (Othman and Benson, 1993). This can significantly affect the material strength, cohesion, and structure of the material, especially in the presence of low stresses (Graham and Au, 1985; Van Vliet-Lanoe and Dupas, 1991). Non-smectite clays, for instance, typically display ice banding in freezing temperatures as pore spaces filled with ice (Van Vliet-Lanoe and Dupas, 1991). On the other hand, bentonites – soils dominated by

montmorillonite – showed no significant lens formation (Anderson and Hoekstra, 1965), but freezing montmorillonite below -5° to -15° dehydrates the clay, resulting in the collapse of the layering structure into a porous aggregate (Anderson and Hoekstra, 1965; Svensson and Hansen, 2010). In these experiments, distinct ice crystals were identified at this transition and their prevalence increased as temperatures were dropped to -50° C; in particular, the presence of ice crystals transformed the system from homogeneous montmorillonite hydrate into the two-phase system of dehydrated montmorillonite and ice, although the layering thicknesses were 2-4 molecules thick (Svensson and Hansen, 2010).

On Ceres, episodic heating early in its evolution or impacts are the only likely freeze-thaw cycle analogs. In the case of smectites, freeze-dehydration can form a porous aggregate instead of the more bonded phyllosilicates structure while producing thin layers of interlamellae ice as well as a general increase in fractures (Pardini, et al., 1996). This could produce both failure planes and reduced friction in some cases while maintaining the typical range of 0.15 – 0.32 coefficient of friction values seen for smectites. In polar latitudes, increases in concentrations of ice or hydrated smectite would produce a more cohesive regolith that results only in failure along particularly steep slopes and to relatively greater depths.

For the ice content of Ceres' overall composition, Prettyman et al. (2017) model the thermal stability depth of ice after 4.5 billion years, which produces equatorial depths to the ice table below the sensing depth of GRaND. As such, hydrogen detected at the equator is not considered to be ice and is subtracted from the polar hydrogen detection to estimate an ice table with 10% ice, which is supported by good matching of the GRaND

data with forward modeled results using 10 wt% water ice, 0.2 porosity, 10 μm grain size, and low diffusivity (Prettyman et al., 2017). Prettyman et al. (2017) further show a possible depth to this table beginning at about 0.9 m depth at the equator and reaching to within centimeters or less of the surface at the poles. Additionally, the latitude determined at which water ice approaches the surface using forward modeling of neutron counting rates is relatively homogeneous in the VIR data, arguing against changes in hydration in the surface layer.

2.4 Landslides on Ceres

Early work on Cerean landslides identified three main flow types by morphology: thick, lobate, and steep snouted Type 1 flows, thin, spatulate long-runout Type 2 flows, and the cusped sheeted Type 3 flows (Buczkowski et al., 2016; Schmidt et al., 2017). This early analyses identified a latitudinal dependence on Type 1 landslides, which combined with their geomorphology, was used as evidence for increased ice content. Values of measured drop height (H) and runout length (L) in the ratio H/L were used to estimate the internal coefficient of friction and suggest an increase in efficiency from Type 1 to Type 2 and Type 3 flows, where ice provides the most consistent mechanism across these features. The range of H/L values from Schmidt et al (2017) are shown in Table 1, along with comparative values for other planetary bodies.

Table 1: H/L value ranges Ceres and other planetary bodies.

Location	H/L Range	Source
Mars, Valles Marineris	0.078 – 0.554	(Quantin et al., 2004)
Iapetus	0.1 – 0.3	(Singer et al., 2012)
Callisto	0.1 – 0.31	(estimated from Singer et al., 2012)
Rhea	0.18 – 0.6	(estimated from Singer et al., 2012)
Ceres	0.06 – 0.42	Schmidt et al., 2017

Type 2 landslides in particular were considered analogous to long runout landslides. Long run-out landslides travel farther than predicted by simple friction models (Evans et al., 2002). Reasons for exceptional distances traveled have been reviewed in multiple places (Shaller and Smith-Shaller, 1996; Legros, 2002), but are summarized below. Explanations have invoked or shown relationships with fluidizing mediums such as air (Fahnestock, 1978; Kent, 1966; Shreve, 1968, 1968b), vaporization of subsurface materials (Goguel, 1978), release of volcanic gases (Voight et al., 1983), and suspension of coarse debris by finer grains (Hsü, 1975). Non-fluid mechanisms include acoustic fluidization (Melosh, 1979), rapid flow spreading (Davies, 1982; Straub, 1997), and self-lubrication (Campbell, 1989; Cleary and Campbell, 1993; Straub, 1996). Additional explanations use continuum models of bulk rheologies (Dade & Huppert, 1998; McEwen, 1989; McEwen & Malin, 1989; Takarada, Ui, & Yamamoto, 1999; Voight et al., 1983), changes in mass (Iverson, 1997), frictional heating causing reduced pore fluid pressure (Vardoulakis, 2000; Voight & Sousa, 1994), and seismic shaking/liquefaction (e.g. Guo, et al., 2014; Iverson et al., 2015).

While each of these could be analyzed individually, the take-away should be that there might be many different mechanisms that influence the ability of a landslide to exceed

frictional modeling, and that individual mechanisms may dominate or work in combination. However, in many of these instances, an underlying knowledge of the environmental factors available can substantially inform of which of those may or may not be applied. For instance, an airless body such as Ceres would not have fluidization via air entrainment. Being volcanically dead and lacking internal heat, the release of volcanic gases or vaporization – at least outside of impact events – can be ruled out. In further instances additional data, such as subsurface radar profiles, can indicate a strong role of subsurface ice, such as was found to be the case for Martian lobate debris aprons (LDA's) (Plaut et al., 2009).

Ceres is the only planetary body with widespread landslides and flows at all latitudes at similar surface environments. This provides a unique look into the relatively homogeneous surface – compared to, say, Mars – and the key ways in which it is not. Specifically temperature differences lead to variation in both near-surface ice content and depth to ice-rich-table. Variability in impact energy and local subsurface properties are among the remaining influences on variation in landslide and flow character. In particular, Ceres is unique for it's ice-silicate composition; silicates include carbonates and phyllosilicates, both weak materials even before mixture with ice. Mars may be the closest analog, with identified subsurface ice in some areas, and even associated with some flow features – in particular the LDAs. However, ancient climate and atmospheric conditions are among the many ways in which Mars is a poor analog. It may be that Ceres is simply our best example of what is more common in the main asteroid belt and in ancient planetary bodies, and for now is the only one with high-resolution imagery.

This will become of particular relevance and interest with the newly selected Discovery missions Lucy and Psyche set to explore other asteroids.

CHAPTER 3: METHODOLOGY

3.1 Data and Tools

Multiple tools and several data products are used in this thesis. The resolution and software used with each dataset or product is summarized in Table 2 below. Image analyses pull from the Framing Camera (FC) (Sierks et al., 2011) instrument and products are derived from those, with resolutions are listed in Table 2. General mapping and spatial geometric analyses utilize the publically available Ceres Low Altitude Mapping Orbit (LAMO) Basemap while topographic measurements use a modified version of the High Altitude Mapping Orbit (HAMO) derived global digital terrain model (DTM) created by Frank Preusker (Preusker et al., 2016) that accounts for the significant flattening along Ceres' polar axis (891 km vs. 965 km and 961 km for the two equatorial axes).

Table 2. FC image and DTM resolutions.

Dataset or Product	Resolution (m/pixel)
HAMO Images	~140
LAMO Images	~35
0-Level Global DTM	Lateral: 137; Vertical: 10

We primarily use GIS ArcMap 10.5 and the additional extensions for 3D Analyst and Spatial Analyst for landslide measurements, but supplement this data as needed with work in USGS ISIS using tools not available in ArcMap. USGS ISIS is used to process individual Dawn FC images and measure precise shadow heights; Processing uses level 1b .img files and converts to .cub, attaches spice kernels, and if needed projects the image

for import into ArcMap. Measurements in ArcMap first apply an Azimuthal Equistant reprojection centered at the feature of interest to ensure accurate values, and heights and distances are extracted from drawn profiles.

3.2 Morphology and Categorization

Cerean landslides exhibit a continuum of behaviors beyond the initial T1 and T2 categories from Schmidt et al., (2017). To highlight any differences in behavior, we apply stricter criteria for classifying T1 and T2 than was used in our previous work (Schmidt et al., 2017) and refer to as intermediate (IM) those features exhibiting characteristics not clearly T1 or T2 and that we partially investigate here. Figure 2 shows two panels of three images for T1 and T2 flows, highlighting first a good example, then a more obfuscated example, and finally a flow that while part of another category might be mistaken as part of the same group. Those landslides remaining in the T1 and T2 categories therefore best exemplify our new, stricter class-defining morphologies and allow us to: (1) better evaluate underlying end-member mechanisms driving the formation of landslides on Ceres, and (2) investigate whether a difference in material behavior could be resolved.

We identified T1 landslides as those that have a steep and rounded snout in the deposit, show little evidence of spreading transverse to the flow between the source and deposit, and initiate on steep slopes. T2 landslides, by contrast, are characterized as long runouts with distinct margins and termini. IM landslides may exhibit characteristics of both, such as a prominent head scarp and steep slope initiation typical of T1 but without a steep snout.

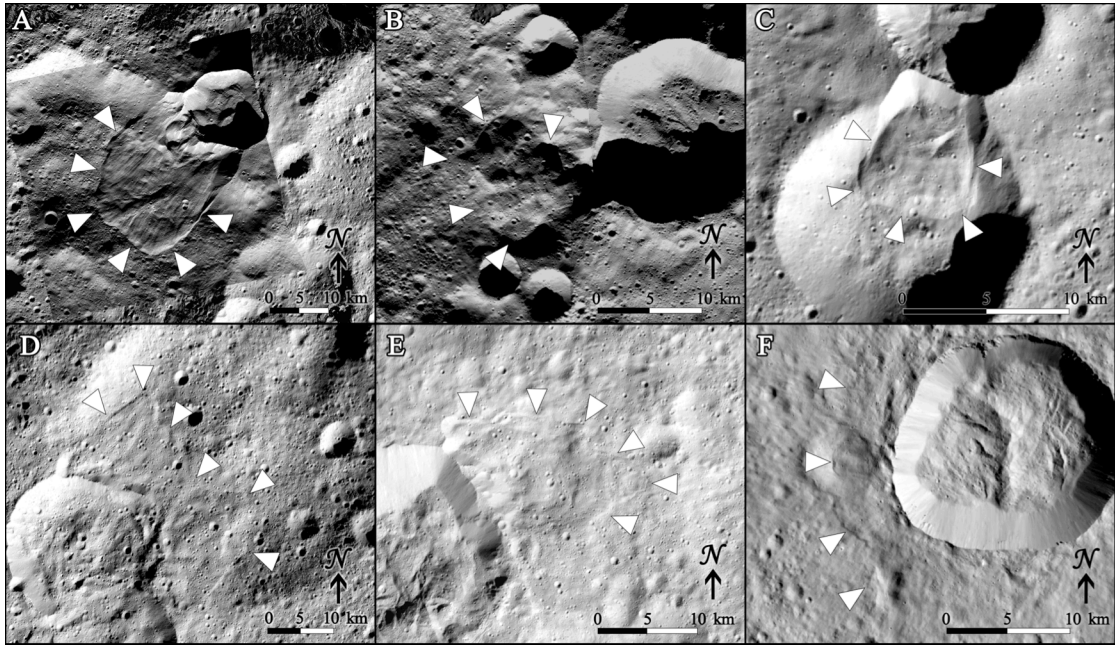


Figure 2. Examples of T1 and T2 with counter examples: **(a)** A clearly visible T1 landslide with characteristic lobate morphology; **(b)** a degraded T1; **(c)** an IM landslide as a counterexample, showing the type of feature excluded from the T1 or T2 classes due to lack of archetypal rounded toe; **(d)** a clearly visible T2; **(e)** a more degraded, subtle T2; and **(f)** a T3 flow as a counterexample, identified by the radial character and surface texture and lack of distinct failure scarps.

There are 43 major T1 and T2 landslides with distinct boundaries making for relatively easy identification and measurement. Of these, three are part of a landslide complex where distinct flows can be individually measured. Another 115 flows and/or key flow observable portions of flows have been mapped into the IM category, although some flows can have multiple events or overlapping failures.

A small handful of landslides and flows are not sourced from small craters on high topography, which is typically a larger, older crater rim. Landslide failure associated with craters could in some situations be connected to the impact, providing initiation energy, so could be somewhat different than those that are not sourced from craters. However, it

is not apparent if there is a way to differentiate among those failures that are a result of the impact and those that occur later due simply to slope destabilization. Additionally, not all small craters on high topography produce a flow, suggesting non-ubiquitous conditions are required for flows to occur, whether that is impact speed, slope angle local ice content, or a combination of these and/or other factors. Finally, for Types 1 and 2 a distinct scar is often present, but this area is not always large or easily identifiable.

3.3 Quantification and Measurements

3.3.1 H/L

Particularly in planetary research, quantification of landslides commonly uses the ratio of the landslide's drop height H and runout length L to establish the ratio H/L , which provides an effective coefficient of friction. This ratio is a coarse reflection of the degree to which a landslide's initial potential energy is converted to kinetic energy during the flow. In essence, it represents the conversion of potential energy to work across some length, which is lost to irrecoverable forms.

$$mgH = mgRL$$

$$H/L = R$$

(1)

Here gravity g and mass m cancel, leaving the ratio of height and length, H/L equated to a resistance coefficient R (Iverson, 1997). A first order treatment attributes the loss to friction. For clarity, there are three types of friction: 1) static friction, which occurs between unmoving objects, 2) dynamic or kinetic friction, which occurs during motion of

a mass on a surface and is generally less than the peak static friction, and 3) internal friction, which is the intrinsic friction of a mass resisting deformation. The simple physics approach for friction is a mass on a surface or slope: For a mass m on a slope of angle θ , the net force F_{net} is defined as

$$\begin{aligned} F_{net} &= mg \sin \theta - \mu mg \cos \theta \\ \mu &= \tan \theta \end{aligned} \quad (2)$$

where g is the force of gravity and μ is the coefficient of friction. Up until the moment of slope failure, the net force is 0, and the coefficient of friction – the static friction – is equal to $\tan\theta$, or H/L . Coefficient of friction values can range substantially depending on whether static or dynamic values are measured and the relevant factors including velocity, overburden, the materials involved, surface roughness, and more. Example values from the literature are shown in Table 3. Note that in the cases of ice at various temperatures, there is a more complicated behavior dependent on overburden, velocity, and temperature. Although no specific study was found, many suggest a friction value of 0.6 for rocks in general (e.g. Goodman, 1980). Ice in particular range from 0.05 – 0.8, depending on conditions (Kennedy et al., 2000; Mills, 2008), while saturated and dry clays range from 0.12 – 0.4 (Behnsen and Faulkner, 2012).

Table 3: Relevant material friction coefficients.

Slope-Mass Material	μ ($\sim H/L$)	Source(s)
Ice-ice (near 273K)	0.05	Mills, 2008
Ice (233 – 270K)	0.05 – 0.8	Kennedy, et al., 2000
Montmorillonite (Smectite)	0.12 (wet) – 0.39 (dry)	Behnsen and Faulkner, 2012
Lizardite (Serpentine)	0.29 (wet) – 0.35 (dry)	Behnsen and Faulkner, 2012
Illite (TOT Clay)	0.38 (wet) – 0.40 (dry)	Behnsen and Faulkner, 2012
Talc (TOT Clay)	0.18 (wet) – 0.22 (dry)	Behnsen and Faulkner, 2012
Muddy Shale	0.25	Goodman, 1980
Georgia marble	0.42	Goodman, 1980
Berea sandstone	0.45	Goodman, 1980
Chalk	0.50	Goodman, 1980
Indiana limestone	0.63	Goodman, 1980
Sioux quartzite	0.70	Goodman, 1980
Stone Mt. granite	0.73	Goodman, 1980

We measured H/L with two approaches. First, we measured the maximum possible values for both drop height (from the top of the scarp to the lowest point at the distal end of the deposit) and length (from the head scarp to the distal end of the deposit). The ratio inferred from these measurements, known as the *Fahrboschung* angle (Heim, 1932) or angle of reach (Voight et al., 1983), is designated here as H_{Max}/L_{Max} . As an effective coefficient of friction, this angle of reach underestimates the kinetic energy of the flow compared with using the center of mass of the flow sliding down a slope (Cruden & Lucchitta, 1980; Voight et al., 1983; Legros, 2002; de Blasio, 2011). Therefore, we also measured H/L from estimates of each landslide’s center of mass (CoM). We visually estimate the center of mass of both the scar and the deposit from a representative topographic profile of the current landslide topography overlain on a profile of nearby, undisturbed topography, typically a close site within or along the same crater rim. We denote the ratio inferred from these measurements as H_{CoM}/L_{CoM} . Although more

subjective than other methods of determining the CoM, this method was more robust due to a variety of issues encountered during topographic data interpolation. These complications primarily arise from irregular or curved topography close to the landslide and in particular interpolation skewing from unequal weighting from nearby upslope and downslope contributions.

Using H/L to quantify the friction value for a landslide has the advantage of being rather easy to measure using the remote data available in planetary settings. However, some significant problems arise due to (1) strong velocity and temperature dependence for low-pressure and independence for high pressure for cold and warm ices (Schulson and Fortt, 2012), (2) a maximum height and length is commonly used instead of the more accurate center of mass (Legros, 2002), (3) the complicated range of possibly interacting mechanisms and the inclusion of impact response for planetary landslides, and (4) the large orders of magnitude covered by length and not height, which results in height values adding scatter to plotted relationships (Legros, 2002). However, used in combination with other approaches, we can build a robust picture of Ceres' subsurface.

3.3.2 V-A:

Recent work has shown that many terrestrial landslide scars follow power-law relationships between the area (A) and volume (V) (Larsen et al., 2010).

$$V = \alpha A^\gamma \quad (\text{Eq. 1})$$

Larsen et al. (2010) observed that bedrock landslides tend to be thicker than soil-based landslides, with typical γ values of 1.3 – 1.6 for bedrock landslides and 1.1 – 1.3 for soil-

based landslides. It is worth noting that a value of $\gamma = 1.5$ would reflect self-similar scaling, the only condition where the depth scales by a factor of α to the square root of the area – or simply put, equivalent to scaling a cube in the case of $\alpha = 1$. We mapped the area of each landslide scar and use the deposit volume as a first-order approximation for landslide scar volume to assess whether Cerean landslides follow a similar power-law relationship and if T1 and T2 landslides behave differently.

Mapping landslides on Ceres carries uncertainties because the full scar area is not apparent in every scar. This is partly due to variable topographic obscuration from the landslide deposits and indistinct lateral boundaries, and partly due to observational limitations resulting from image resolution (~ 35 m/pixel) and poor lighting conditions. To demonstrate the size of these uncertainties, we measure the minimum and maximum scar areas as well as report “preferred” values based on our best estimates (See Appendix A).

We measure minimum scar areas based only the obviously exposed scarps. To estimate the maximum scar area, we measure an area that extends longitudinally from the head scarp to the deposit toe and laterally from the scarp walls and deposit boundaries. While this likely overestimates of the scar area, this presents a robust upper limit. Our preferred scar area estimate extends from the crown of the head scarp to the approximate start of the crater floor, and is laterally bounded by the scarp sides and deposit margins. This provides a consistent metric that considers the visibly disturbed material and extends downslope until the break in slope near the crater floor.

Scar volume is difficult to measure in many of our mapped landslides due to partial obscuration of the scars and resolution limitations, so we approximate scar volume by

measuring the volume of the landslide deposit. We estimate deposit volume from the mapped deposit area and by measuring landslide thickness from multiple topographic profiles along the deposit and the same interpolated pre-landslide topography generated in our *H/L* analyses from the Dawn HAMO DTM (Preusker et al., 2016). Deposit volumes should differ from scar volumes to the extent that the landslides exchanged material with the bed, lost volatiles to space, or changed in bulk porosity during transport. Given the observational constraints, we consider the deposit volume to be the best estimate of scar volume. After measuring landslide areas and volumes in this way, we determined γ -values from the volume-area relationship for the T1 and T2 populations to compare the two groups then describe in context of all measured landslides overall.

3.4 Ice Content Analysis

In combination with conclusions of subsurface ice content by Prettyman et al. (2017), we also explore the possible ice content under the conditions that upward water migration or surface removal means the full 4.5 billion years has not yet moved the ice table depth to below the GRaND sensing depth. To do this, we use the VIR and IRFT compositional constraints to make simple calculations from the GRaND WEH (Rivkin et al., 2006; De Sanctis et al., 2015; Ammannito et al., 2016; Prettyman et al., 2017).

From ground-based and VIR spectrally derived compositions and their estimated abundances, we calculate the wt% of hydrogen they contribute, subtract this from the available hydrogen GRaND detected, and identify the amount of ice the remaining hydrogen could comprise (Table 4). To convert the vol% provided by spectral data, we scale the reported percentages by the ratio of the average mineral density to Ceres' crust

bulk density, using the crustal estimate of 1287 kg/m^3 by Fu et al. (2017). Similarly, calculated remaining wt% ice is converted to vol% through the ratio of the crustal density to ice. This explores the assumption that through overturn or other processes, ice could penetrate to within the sensing depth GRaND, even at the equator. We assume that this hydrogen is not present in the spectrally neutral material, which comprises 50-80% of the surface material (Rivkin et al., 2006). In the spectrally non-neutral material, carbonate is estimated to be 4-6% (Rivkin et al., 2006) and phyllosilicates to be 9-21% (Ammannito et al., 2016). Sodium carbonate was also detected in high concentrations at Occator (De Sanctis et al., 2016), so we choose this as the carbonate explored in our mixtures. For the clays, in addition to being relevant components, the molecular structure of cronstedtite and montmorillonite allows for some of the greatest range in hydrogen content, either in the form of OH or H₂O. Smectites in particular have the greatest potential to take up water. To calculate a lower limit on ice content in Ceres' surface materials, we consider an assemblage of 6% sodium carbonate salt and 21% clay composition of saturated montmorillonite (the most water-hungry smectite and H-bearing mineral within observational constraints).

CHAPTER 4: RESULTS

In total, we classified 13 landslides in our T1 endmember group, 29 in our T2 endmember group, and 116 landslides that were classified as T1 or T2 in Schmidt et al. (2017) into the IM group. Our restricted groups of T1 and T2 landslides are consistent with the findings in Schmidt et al. (2017), with T1 landslides concentrated poleward of 70° latitude (aside from two at ~50° latitude) and T2 landslides concentrated equatorward of 70° latitude (Figure 3). We do observe one archetypal T2 type landslide in the north polar region that appears to be a secondary failure associated with a T1 landslide.

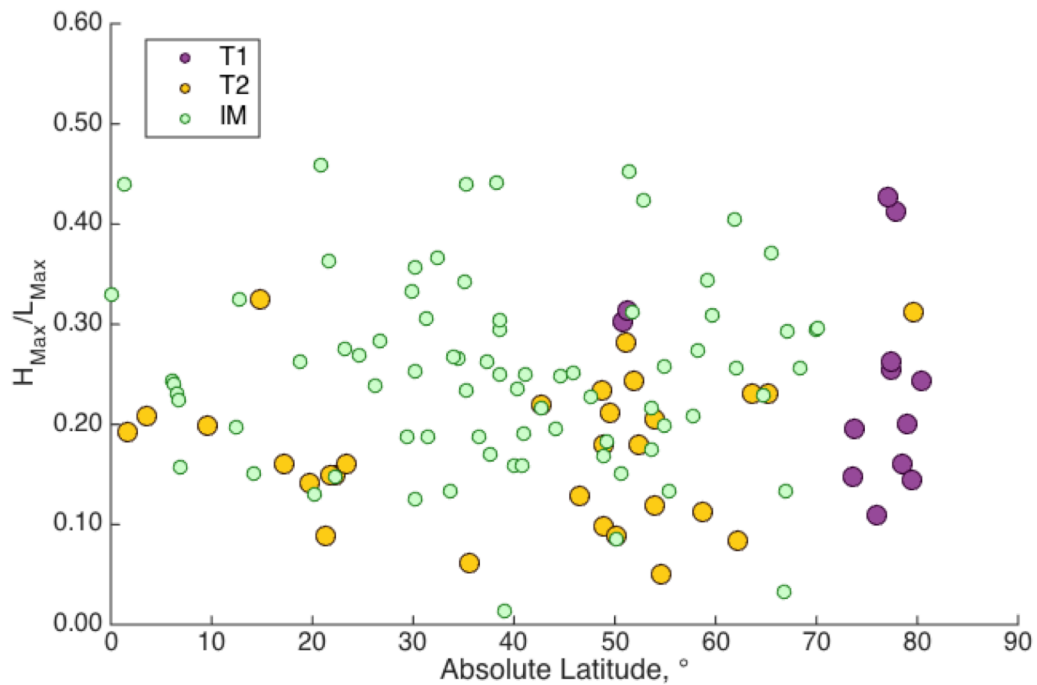


Figure 3. Latitudinal Distribution of Cerean Landslides.

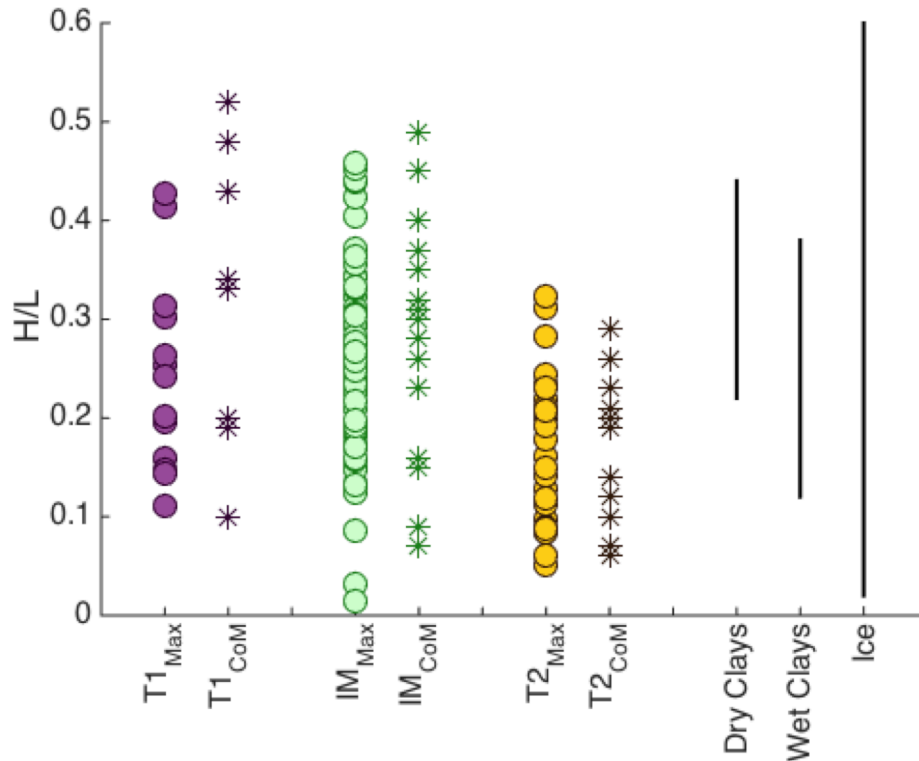


Figure 4. T1, T2, and IM H/L values compared with ranges for clays and ice.

Despite the variation in H/L values with flow type (and hence with latitude), a strong latitudinal dependence on these values is not apparent within flow type. Instead the H/L values reflect only the upward shift of T2 to T1 values at $\sim 70^\circ$ absolute latitude, with IM landslides, which include complex features and those with poor boundaries, demonstrating a larger range even at latitudes below 70° (Figure 3).

4.1 H/L measurements

Max and CoM values for T1, T2, and IM features are compared in Figure 4, along with the span of values attributed to dry and saturated clays and ice across a range of relevant compositions and temperatures from the literature and that was presented in

Table 3. We excluded four T1 and 13 T2 landslides from the H_{CoM}/L_{CoM} analyses because of difficulties estimating the center of mass in these landslides; only 16 landslides were measured for CoM in the IM group. From the max measurements we excluded 41 IM features, often due to unclear boundaries or complex settings.

Numerical means, range, and error are listed in Table 4. CoM all trend to higher means than Max, except for T2 landslides, which overall is in good agreement with conclusions in the literature comparing max and CoM. T1 landslides have H/L values of 0.24 ± 0.10 if inferred from the landslides' maximum extents, and 0.31 ± 0.15 if inferred from their center of mass. These are, on average, higher than H/L values for T2 landslides, which are 0.17 ± 0.07 for both max and CoM; at the significant figures reported these are indistinguishable, although the CoM values are more closely clustered but with 13 fewer measurements and a break centered around 0.17. However, the IM values ($H_{Max}/L_{Max} = 0.25 \pm 0.09$, $H_{CoM}/L_{CoM} = 0.27 \pm 0.12$) and values produced when combining all the landslides together ($H_{Max}/L_{Max} = 0.23 \pm 0.09$, $H_{CoM}/L_{CoM} = 0.24 \pm 0.12$) are more similar to T1 landslides than T2, aside from the combined CoM. The large spread in H/L values in each flow type, however, results in mean values that are indistinguishable from one another within uncertainty.

Our H/L measurements span a range larger than the range of internal coefficients of friction in clays. For example, in a few cases T1 and IM landslides reach H/L values larger than those encompassed by clays, suggestive of a material with a higher effective coefficient of friction than clays. The lowest H/L values in the IM and T2 landslides are lower than the lowest coefficient of friction in clay (a saturated montmorillonite). This suggests that clays alone cannot explain the behavior of the observed flows. Laboratory

measurements of internal friction values for ice, however, range from 0.02 at near melting temperatures (Mills, 2008) to 0.8 at temperatures of 233 K (Beeman et al., 1988), fully covering the range of observed effective coefficients of friction. Incorporating the friction reduction by warm ice or melted ice would allow comparably low coefficient of friction values.

Table 4: H/L and V-A values for Cerean landslides.

<u>Type</u>	<u>H_{Max}/L_{Max}</u>	<u>H_{CoM}/L_{CoM}</u>	<u>Range</u>	<u>α</u>	<u>γ</u>	<u>R^2</u>
T1	0.24 ± 0.10	0.31 ± 0.15	0.11 – 0.52	0.0003	2.00 ± 0.44	0.84
T2	0.17 ± 0.07	0.17 ± 0.07	0.05 – 0.29	0.0026	1.24 ± 0.25	0.73
IM	0.25 ± 0.09	0.27 ± 0.12	0.01 – 0.49	0.0001	1.61 ± 0.22	0.65
All	0.23 ± 0.09	0.24 ± 0.12	0.01 – 0.52	0.0015	1.45 ± 0.17	0.62

4.2 Volume-area measurements

Landslides scar area and volumes are plotted in Figure 5 and values shown in Table 4. We excluded seven T1, 18 T2, and 85 IM landslides from the volume analyses due to difficulties estimating the volumes in these landslides. The best fit γ -value for all Cerean landslides combined sits at 1.39 ± 0.17 , nearly centered at self-similar scaling ($\gamma = 1.5$). For T1 landslides, the best-fit value is $\gamma = 2.00 \pm 0.44$, which is above self-similar scaling to within one sigma and is significantly higher than the γ value in terrestrial bedrock landslides (1.35 ± 0.01 ; Larsen et al., 2010). For T2 landslides, $\gamma = 1.24 \pm 0.25$, which is below self-similar scaling but still close to self-similar scaling and cannot be distinguished from the terrestrial soil-based landslides (1.145 ± 0.008). The mean value of $\gamma = 2.00$ for T1 is very high compared with the range of terrestrial values and may

suggest something unique is occurring at Ceres. T1 and T2 γ -value means do not overlap within a 1-sigma confidence level, which is consistent with different landslide depth-area relationships between the two flow types. IM landslide values, which overlap with T2 landslides latitudinally, are indistinguishable from either group. This reinforces both the gradational qualities between T1 and T2 landslides and the need to extract the best endmember cases of the T1 and T2 groups to extract relationships with those morphological types. Comparing γ -values to two possible populations was also conducted using latitudinal cutoff of 60° , but the relationship seen with the morphological types or cutoff above 70° latitude was not maintained. We also tested for an H/L cutoff criterion instead of morphological classes. However, such a division result in errors on the scale of the values themselves, suggesting that mobility may also be independent of failure.

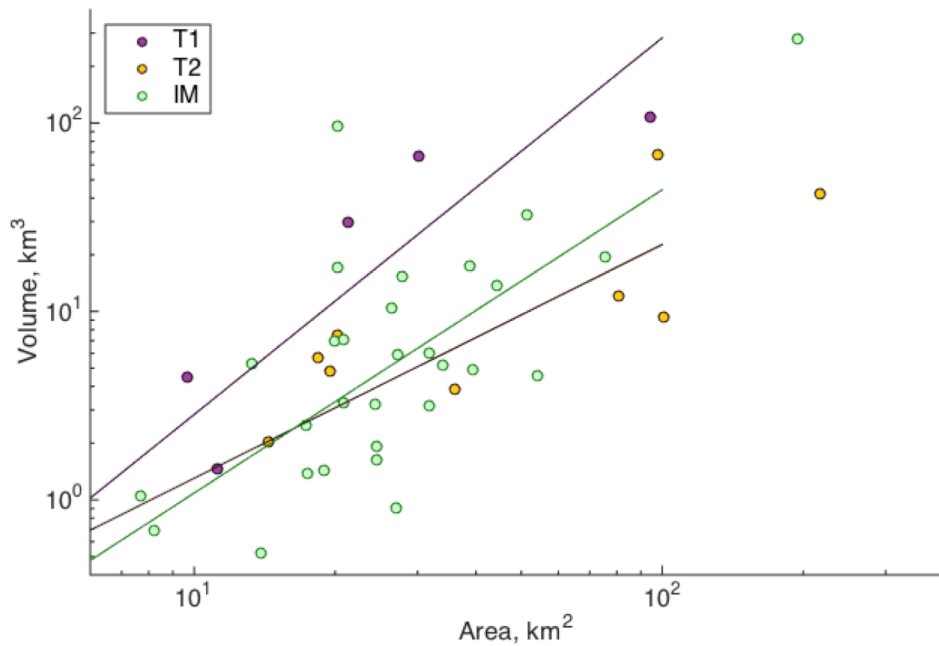


Figure 5. V-A of T1, T2, and IM landslides.

Table 5. Modeled compositions for Ceres' surface materials.

Type	Name	Molecular Formula	Equat. Ice (Wt%)	Polar Ice (Wt%)	Equat. Ice (Vol%)	Polar Ice (Vol%)
Ice	Water ice	H ₂ O	15%	30%	21%	42%
Clays - Smectites	Montmorillonite (dry)	(Ca) _{0.33} Al _{1.12} Mg _{0.56} Fe _{0.28} Si ₄ O ₁₀ (OH) ₂	13.5%	28.5%	18.9%	39.9%
	Montmorillonite (sat)	(Ca) _{0.33} Al _{1.12} Mg _{0.56} Fe _{0.28} Si ₄ O ₁₀ (OH) ₂ ·10H ₂ O	3.4%	18.4%	4.7%	25.7%
	Saponite	Ca _{0.1} Na _{0.1} Mg _{2.25} Fe ²⁺ _{0.75} Si ₃ AlO ₁₀ (OH) ₂ ·4(H ₂ O)	5.1%	20.1%	7.1%	28.1%
	Vermiculite	Mg _{1.8} Fe ²⁺ _{0.9} Al _{4.3} SiO ₁₀ (OH) ₂ ·4(H ₂ O)	7.7%	22.7%	10.8%	31.8%
Clays - Serpentes	Mg-Antigorite	(Mg) ₃ Si ₂ O ₅ (OH) ₄	9.2%	24.2%	12.9%	33.9%
	Fe-Antigorite	(Fe) ₃ Si ₂ O ₅ (OH) ₄	10.7%	25.7%	14.9%	35.9%
	Cronstedtite	Fe²⁺₂Fe³⁺(Si,Fe³⁺)O₅(OH)₄	10.1%	25.1%	14.1%	35.1%
Clays - Other	Talc	Mg ₃ Si ₄ O ₁₀ (OH) ₂	10.7%	25.7%	15.0%	36.0%
	Chlorite	(Mg,Fe,Li) ₆ AlSi ₃ O ₁₀ (OH) ₈	9.4%	24.4%	13.1%	34.1%
Carbonates and other salts	Sodium Carbonate (Hydrated)	Na₂(CO₃)·10H₂O	13.5%	28.5%	18.9%	39.9%
	HydroMagnesite	Mg ₅ (CO ₃) ₄ (OH) ₂ ·4H ₂ O	13.0%	28.0%	18.2%	39.2%
	Epsomite	MgSO ₄ ·7H ₂ O	12.2%	27.2%	17.1%	38.1%
Others	Brucite	Mg(OH) ₂	6.4%	21.4%	8.9%	29.9%
Combinations	4% sodium carbonate (hydrated), 9% Cronstedtite		11.9%	26.9%	16.6%	37.6%
	4% sodium carbonate, 9% Montmorillonite (dry)		13.4%	28.4%	18.7%	39.7%
	4% sodium carbonate, 9% Montmorillonite (sat)		9.0%	24.0%	12.6%	33.6%
	6% sodium carbonate (hydrated), 21% Cronstedtite		8.6%	23.6%	12.0%	33.0%
	6% sodium carbonate, 21% Montmorillonite (dry)		12.1%	27.1%	16.9%	37.8%
	6% sodium carbonate, 21% Montmorillonite (sat)		1.9%	16.9%	2.6%	23.6%

4.3 Constraints on ice content using compositional constraints

The selected assemblage would allow for 3 vol% ice at the equator and 24 vol% of the polar ice. Using the same method for other model assemblages, the upper limits for ice content would be 19 vol% ice at the equator and 40 vol% at the poles; other clays of interest produce values between these endmembers while salts such as hydromagnesite or the fully hydrates magnesium sulfate epsomite instead of sodium carbonate decrease the estimated ice content by 1.5 vol% or less. If we enforce a constraint of no ice in our calculations, then mixtures of dehydrated sodium carbonate and montmorillonite do not contain enough hydrogen to reproduce the GRaND WEH results at the poles, although equatorial values are reasonable if higher than reported spectral observations. For saturated mineral compositions at the poles, end-member conditions require 21 vol% or 51 vol% montmorillonite and 74 vol% or 6% sodium carbonate to reproduce GRaND hydrogen results, well above what is observed spectrally (Ammannito et al., 2016; Prettyman et al., 2017; Rivkin et al., 2006). However, if hydrogen is associated with the spectrally neutral components, specifically brucite (Milliken and Rivkin, 2009; Zolotov, 2016), only 3-21 vol% would be necessary at the equator to account for the GRaND detection, depending on whether montmorillonite is taken as hydrated or dehydrated.

Minimum ice content can be considered from three stances: 1) mid- to low- latitude landslides reflect the 10 wt% ice content proposed by Prettyman et al. (2017), below which a higher ice content layer persists and nears the surface at polar latitudes but remains below GRaND sensing depth, 2) as previous, but ice content increases with depth within the mid- to low-latitude layer with a distinct underlying layer of even higher ice content, or 3) due to either upward water migration or surface material removal, ice

subsurface ice younger than a few billion year old allows for GRaND WEH results to reflect some ice content even at equatorial latitudes. Interestingly, the lower bound on ice content in these cases is relatively similar, from the 10wt% ice content from Prettyman et al. (2017) and 8 – 14% for case 3. The upper limit on ice content suggested by crater morphologies is 30 - 40% water ice by volume, although higher than 40% ice may be present in the form of clathrates, but the existence of such materials is poorly constrained (Bland et al., 2016).

CHAPTER 5: CONCLUSIONS

Landslide H/L values are thought to reflect landslide kinematics, and our H/L measurements on Ceres are consistent with relatively low effective coefficients of friction for the observed landslides. Failure characteristics are also at least partially dependent upon the materials involved, which can further elucidate the conditions governing failure. In terrestrial studies of landslide scars, for example (Larsen et al., 2010), the depth of soil-based landslides does not increase with failure area as quickly as it does in bedrock landslides, implying a limit on landslide volume imposed by soil depth. This distinction offers the opportunity to identify the presence of layers of different shear strength, reflected in the internal coefficient of friction and cohesion. Thus, analyzing the behavior of potential subsurface materials under failure and kinetic conditions together can provide constraints and insights into the regolith and shallow subsurface of planetary bodies.

The effective coefficient of friction, estimated by H/L , approximates the internal coefficient of friction of the landslide materials to a first order. As such, we prefer interpretations that invoke materials that have internal friction values that span the full range of H/L measurements on Ceres to be present in the subsurface. The lowest H/L values observed in Cerean landslides are lower than the lowest effective friction angles in hydrated clays in laboratory experiments. This is consistent with an enhancement in mobility in Cerean landslides via warm ice or melt-water, such as might be produced by impact heating or ice grain heating during sliding as reported in Schmidt et al. (2017). The hypothesis that ground ice is pervasive is consistent with the prevalence of T1 landslides at higher latitudes is thus still consistent with our analyses, and does not

require appealing to new materials or conditions. Low mobilities below 70° latitude in IM landslides may reflect a more complex subsurface and localized regions of higher ice content – colder ice temperatures should reflect the latitudinal temperature gradient and so are less likely to be the contributing factor in those high H/L values.

Like our H/L measurements, our landslide volume and area observations may reflect the subsurface material properties. As described in Section 3, for our measurements of landslide volume we make the simplifying assumption that the deposit and scar volumes are equal, which is equivalent to assuming that neither the landslide mass nor its bulk porosity change during transport. Our volume-area analyses are therefore subject to uncertainties associated with this assumption, as well as to measure uncertainties in mapped scar areas.

T2 landslides have γ -values significantly below the self-similar scaling value of 1.5 such that even though failure areas are often higher for T2 landslides, the failure depth remains relatively shallow, perhaps indicating a weaker layer failing above a stronger one. T1 landslides have a higher γ -value than T2, and are near or above self-similar scaling, indicating that as the failure area increases, an equivalent or greater increase in excavation depth also occurs. This is broadly consistent with a subsurface in which shear strength does not vary strongly with depth, such that there is no strong preference for depth of failure. This suggests the depth-limited properties of the subsurface found from T2 flows are either minimal or not present at the higher latitudes where T1 landslides are found. These results suggest that at mid- to low latitudes, a weaker material both overlies a somewhat stronger material at depth and thins significantly towards the poles. It is

unknown if such layering would be within the regolith or between the regolith and an icy bedrock at Ceres.

However, the presence of IM landslides – which have higher γ -values that overlap with T1 landslides within one sigma – at latitudes below 70° may indicate a more complex environment. One explanation is that there are strong local variations in this weak layer. Another possible explanation is that the T2 landslides isolated here fail under more unique conditions that allow for depth-limited behavior. A third possibility is that this weak layer is better described by a gradient between two layers of somewhat close shear strengths, which is consistent with ice-influenced bulk material properties and a temperature gradient with depth from a warmed surface is. These are not exclusive of each other.

Studies of frozen silt and clays show that bulk strength increases with decreasing temperatures (Yuanlin & Carbee, 1984; Li, et al., 2004; Christ & Kim, 2009). Polar conditions at Ceres would then be expected to increase the strength of any ice rich materials, which is consistent with the distribution and both failure and kinetic behaviors observed in T1 landslides. Ice mixtures noticeably decrease in strength at 60% - 70% ice by volume or more, but there is little data to suggest how this is affected by changes in temperature (Ting, et al., 1984; Arenson, Johansen, & Springman, 2004). Colder ice also has a higher coefficient of friction than warm ice or clays, which could promote more sluggish landslides in those conditions as we observe. Therefore we interpret the deep failure of T1 landslides as consistent with the hypothesis that these features formed in ice-rich materials near Ceres' surface.

This change in ice content would approach the surface near the poles, which is consistent with GRaND data indicating an increase poleward of WEH; the lack of VIR interpretations above 60° latitude (typically due to complications with reflectance models at high incidence angles) does not provide good constraints on an increase in hydration state or ice content at the surface at high latitudes (2017).

Smectite clays, which can contain variable amounts of water, could explain some of the hydrogen uptake in the form of both OH and H₂O. However, ice exposures on the surface (Combe et al., 2018) indicate this would need to be paired with localized ice deposits. For the WEH to be entirely explained by clays, the clay would need to be fully saturated and comprise nearly 80% of the surface material at the poles. Such a scenario is highly unreasonable since spectral analysis indicates phyllosilicate abundances of only a few tens of percent. Other clays, notably serpentines that might be expected to form on Ceres due to its likely chondritic starting composition, do not have as great a capacity to take up water as smectites. Regardless, ice abundances of at least ~10% are needed to account for the GRaND detections unless other minerals take up significant portions of the surface composition – for example sodium carbonates would comprise ~24% of the surface material. Hydrated salts, brucite, and similarly simple compositions where hydrogen is a major proportion of the molecular weight provide the easiest pathway to account for the hydrogen detections from GRaND without invoking ice.

Our analyses of cerean landslides provide insight into the properties of mobilized surface and subsurface material and their influence on landslide failure, transport, and deposition. Our *H/L* and volume-area measurements in combination with observations from VIR and GRaND contribute to a more complete and detailed picture of the upper

few kilometers below Ceres' surface; The collection of geomorphic and compositional data is consistent with an ice-poor regolith layer that is thick at mid- to low-latitudes and thins out at $\sim 70^\circ$ latitude and which overlies an ice-rich layer of $\sim 24\text{-}40\%$ ice (Figure 5). From VIR data, the outermost desiccated “lag layer” must be at least a few mm thick and could extend to the full thermal stability depth as presented in Prettyman et al. (2016). Except at the poles, our work suggests that below the ice-free lag layer exists a layer with intermediate ice content up to a few hundred meters thick.

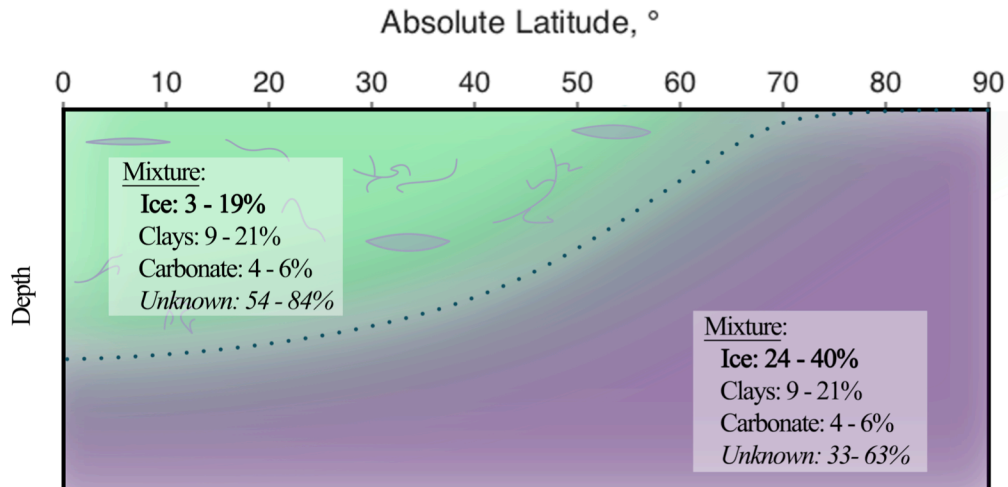


Figure 6. Suggested subsurface structure and composition for Ceres as a function of latitude.

Such a layer would contain $\sim 3\text{-}19\%$ ice in possibly the form of lenses and interstitial or fracture-lined films, possibly with hydrated mineral species. A comparatively ice-rich layer comprised of at least 23% and up to or greater than 40% ice, may lie below these layers and is near or exposed at the surface at polar latitudes. It is likely that the depth boundary between the ice-depleted layer and the ice-rich layer is diffuse rather than sharp

due to the variability seen in the data, and the difference in shear strength between these layers is not high. Such a weakly layered structure is consistent with the latitudinal dependence of landslide behavior, where low-mobility T1 landslides that can fail to greater depths are found only where the subsurface properties are relatively uniform, while both the high-mobility T2 landslides that have depth-limited failures and the IM landslides with diverse mobilities and a moderate relative failure depth are found where there is a layered subsurface structure. The inferred ice contents are consistent with the GRaND data (Prettyman et al., 2017) and with detection of exposed ice by VIR, often associated with landslides (Combe et al., 2018), and with previously calculated latitudinally varying ice table depths (Hayne & Aharonson, 2015; Prettyman et al., 2016; Schorghofer, 2016; Landis et al., 2017).

A layered crustal model may also explain additional Cerean features such as scalloped craters, lumpy crater deposits, and exposed ice in areas of crater wall failure (Formisano et al., 2017; Schmidt et al., 2017; Combe et al., 2018). Local heterogeneities might be responsible for some of the variability within T2 flows, including thinner, more mobile T2 flows that are seen at somewhat high latitudes. Further, the IM landslides that demonstrate properties of both T1 and T2 landslides. Overall, a shallow layer of clays lensed with ice in the mid- and low-latitudes in the top few kilometers of Ceres is consistent with our landslide observations in this study.

APPENDIX A: KEY DATA

TypeID	Location		$\Delta H/\Delta L$		$\Delta H/\Delta L$		Scar	Deposit
ID	Lat, °	Lon, °	Max	error	CoM	error	Pref. Area, (km ²)	Vol. (km ³)
IM_ne w	-53.603	-84.296	0.174				- (? – 82.2)	
IM_ne w2	12.500	-116.089	0.197					
IM_ne w3	-55.376	124.973	0.134	0.004	0.15		473.3 (67.8 – 966)	393
IM001	57.819	86.110	0.209	0.007	0.26	0.058	31.8 (12.9 – 52.4)	5.97
IM002	34.416	37.783	0.266	0.008	0.35		4.8 (0.44 – 7.8)	0.126
IM003	66.960	26.350	0.134	0.002	0.15	0.056	17.5 (.5 – 28.8)	1.385
IM004	66.725	25.462	0.032	0.001	0.07		- (? – 2.3)	
IM005	67.106	25.620	0.293	0.043	0.32		5.7 (1.7 – 10.2)	
IM006	69.920	24.783	0.294	0.001	0.35		27.3 (11.6 – 41.2)	5.87
IM007	68.359	26.426	0.256	0.006	0.30		19.9 (10.5 – 38.3)	6.914
IM008	61.933	52.165	0.404	0.020	0.49	0.099	17.4 (11.1 – 31.5)	2.49
IM009	58.153	56.327	0.274	0.006	0.31	0.112	13.3 (4.8 – 26.6)	5.325
IM010	50.118	-124.308	0.086	0.013	0.09		75.4 (32.3 – 208)	19.405
IM011	-50.556	3.822	0.151	0.029	0.16		16.9 (3.5 – 62.7)	
IM012	62.103	-105.502	0.256	0.013	0.23		29.7 (14.9 – 117)	
IM013	26.293	14.668	0.239	0.002	0.28		30.5 (9.3 – 89.7)	
IM014	35.261	48.523	0.234	0.014	0.45		41.1 (11.9 – 65)	
IM015	32.373	47.640	0.366	0.100	0.37		4.1 (4.1 – 11.5)	
IM016	-6.132	115.651	0.243		0.16		27.9 (12.4 – 73.6)	15.3
IM017	49.204	169.713	0.183				2.9 (1.9 – 4.8)	
IM018	60.027	158.114						
IM019	52.912	146.574	0.423				8.2 (5.8 – 13.6)	
IM020	-44.165	173.687	0.195		0.40		- (? – 317)	
IM021	-38.253	173.127	0.441					
IM022	-40.666	168.397						

IM023	-35.271	168.058	0.439					4.74
IM024	-39.743	176.858						
IM025	59.590	333.149	0.308				34.1 (25.4 – 51.5)	5.22
IM026	59.216	334.568	0.344				18.9 (15.3 – 29.6)	1.43
IM027	29.393	-51.816	0.187				194 (98 – 330)	278.4
IM029	36.513	299.381	0.187				38.9 (17.6 – 72.2)	17.57
IM030	6.299	-13.546	0.240				24.5 (12.8 – 51.2)	1.92
IM031	35.060	-7.151	0.342				8.7 (5.2 – 14.3)	
IM032	45.923	-76.056	0.252					
IM033	12.715	-24.906	0.324				7.2 (1.3 – 15.5)	
IM034	26.180	-25.800						
IM035	51.734	-44.745	0.312				5.5 (4.1 – 15.6)	
IM036	35.380	-55.070						
IM037	6.618	359.360	0.231					
IM038	26.754	-60.675						
IM039	60.776	-110.974						
IM040	63.314	-109.451						
IM041	62.801	-109.590						
IM042	62.811	-109.942						
IM043	18.728	-125.599	0.263				13.7 (8.8 – 33.3)	
IM044	32.637	-135.144						
IM045	30.111	-138.888	0.356				4.8 (4.2 – 6.1)	
IM046	18.298	-144.384					3.7 (1.9 – 6.1)	
IM047	48.864	-131.300	0.168				54 (36 – 98.9)	4.572
<i>IM048</i>	<i>44.190</i>	<i>-74.799</i>						
IM049	1.303	-100.921	0.440				3 (1.5 – 5.2)	
IM050	62.026	-138.344					- (? – 21)	
IM051	51.408	-79.901	0.452				27 (25 – 31)	0.9
IM052	30.151	-90.976	0.253				31.9 (25 – 60.1)	3.17
IM053	-0.113	-107.591	0.330				1.8 (1.4 – 2.6)	
IM054	1.808	-108.726					4.2 (2.5 – 6.5)	
IM055	64.732	-77.441	0.229				20.2 (4.7 – 56.2)	96.5

IM056	65.532	-81.686	0.371				7.8 (4 – 26.6)	
IM057	25.724	-106.381					0.6 (0.2 – 1.3)	
IM058	12.500	-116.089						
IM059	5.624	-118.962						
IM060	5.483	-118.975						
IM061	4.843	-121.876						
IM062	3.536	-123.944						
IM063	7.364	-121.333						
IM064	46.975	-120.515						
IM065	33.952	-128.034						
IM066	3.117	-144.896						
IM067	3.155	-144.701						
IM068	9.452	-160.780						
IM069	31.350	-97.581	0.306				51.4 (25.8 – 69.3)	32.85
IM070	20.849	7.933	0.458	0.022			6 (4.8 – 7.2)	
IM071	29.911	0.371	0.332				44.2 (33.8 – 68.3)	13.8
IM072	-47.668	19.152	0.227				9.5 (7.6 – 16.9)	
IM073	-38.587	48.521	0.295				6.3 (4.6 – 34.6)	
IM074	14.255	79.938	0.151				170.6 (32.4 – 329)	
IM075	20.690	101.432						
IM076	6.720	88.859	0.225				13.9 (10.9 – 17.9)	0.525
IM077	-70.169	2.858	0.296				39.3 (27.2 – 51.8)	4.92
IM078	-35.499	167.575						
IM079	26.772	131.083	0.283				24.3 (16.3 – 37.7)	3.21
IM080	-3.356	144.199						
IM081	-24.628	136.960	0.269				20.8 (14.7 – 47.6)	3.29
IM082	22.328	160.488	0.148					
IM083	20.248	159.686	0.130					
IM084	20.031	159.745						
IM085	6.888	149.965	0.157				26.4 (14.5 – 68.1)	10.475
IM086	-23.269	57.154	0.276				14.4 (6.3 – 27.8)	
IM087	-42.752	45.781	0.217				20.8 (14.9 – 62.3)	7.11
IM088	33.771	95.668						
IM089	37.875	86.312						

IM090	24.185	19.119						
IM091	-30.258	-156.166	0.125				6.3 (5.1 – 9.5)	
IM092	-38.531	-93.608	0.304				8.1 (2 – 17.4)	
IM093	-39.021	-94.066	0.014				8.2 (4.8 – 18.5)	0.685
IM094	-39.963	-94.885	0.158					
IM095	-40.273	-95.305	0.235					
IM096	-40.873	-95.814	0.159					
IM097	-41.086	-96.317	0.249					
IM098	31.411	-69.909	0.188				3.8 (2 – 6.7)	
IM099	-37.330	177.154	0.263				44 (29.2 – 58.1)	
IM100	-38.568	178.237	0.250				33.6 (17.5 – 33.9)	
IM101	-37.607	178.663	0.170				24.6 (17.5 – 33.9)	1.64
IM102	21.679	-167.953	0.363				8.3 (7.1 – 11.4)	
IM103	-44.578	153.337	0.248				61.6 (32.9 – 104)	
IM104	-40.926	111.953	0.191				44.9 (10.9 – 96.9)	
IM105	54.898	73.614	0.257					
IM106	-77.413	165.034						
IM107	-43.034	38.013						
IM108	-34.055	90.876	0.268				7.7 (4.4 – 21.8)	1.044
IM109	54.359	95.147					74.6 (68.8 – 171)	
IM110	67.998	-97.203						
IM111	-53.603	-84.296	0.217	0.029			122.7 (10.5 – 45)	
IM112	-54.894	-84.616	0.198				31.5 (9.1 – 53.5)	
IM113	-7.604	-139.476						
IM114	-33.714	-95.599	0.133				20.2 (3.3 – 72.3)	17.25
IM115	58.520	-96.871						
T1_01	75.943	-99.944	0.110	0.002	0.10		116.9 (47.7 – 208)	
T1_03	50.804	27.326	0.302	0.002	0.33	0.050	11.2 (5.8 – 38.8)	1.455
T1_04	78.530	38.822	0.160	0.005	0.20	0.068	94.1 (50.2 – 411)	108.21
T1_05	-77.331	165.665	0.254	0.003	0.43	0.134	? (8.9 – 88.9)	12
T1_06	-77.398	163.818	0.263	0.002			16.7 (7.2 – 30.5)	

T1_07	-77.847	166.295	0.413	0.003	0.52		16.1 (7.2 – 33.1)	
T1_08	-77.094	161.717	0.427	0.003			9.7 (7.7 – 30.5)	4.5
T1_09	80.437	-6.451	0.243	0.001			46.2 (4.8 – 120.8)	
T1_10	73.627	30.523	0.148	0.005	0.48		-	
T1_11	51.274	-43.939	0.313	0.020	0.34		5.9 (3.62 – 14.6)	0.55
T1_12	-73.814	-108.643	0.196	0.007	0.19		21.3 (10.9 – 126)	29.825
T1_13	79.392	-121.222	0.144	0.013			156.8 (16.7 – 351)	
T1_14	78.999	-3.414	0.201	0.005	0.19		30.1 (12.1 – 115)	67.179
T2_02	9.647	-64.202	0.199	0.003			20.3 (9.3 – 46.7)	7.48
T2_03	46.508	-69.730	0.129	0.004	0.12	0.048	101.1 (27 – 217.8)	9.415
T2_05	17.271	-16.384	0.161	0.008			11.2 (3.2 – 25.5)	
T2_06	62.268	-102.545	0.083	0.003			-	
T2_08	54.570	-104.046	0.051	0.005			-	
T2_10	42.686	-74.181	0.219	0.003			127.5 (5 – 297.4)	
T2_12	49.503	-90.596	0.211	0.014			17 (5.2 – 42.8)	
T2_13	48.895	-90.924	0.179	0.005	0.26		-	
T2_15	48.915	-119.372	0.098	0.003	0.07		48.9 (12.8 – 111)	
T2_18	51.030	26.076	0.282	0.006	0.26		8.5 (3 – 20.8)	0.3
T2_19	22.256	17.484	0.149	0.002	0.23		36 (10.3 – 82.7)	3.835
T2_20	23.378	17.533	0.161	0.002	0.14		43.6 (4.6 – 90.9)	
T2_22	79.620	39.112	0.312	0.033	0.29		14.4 (7.4 – 44.8)	2.03
T2_23	53.928	126.680	0.205	0.001	0.20	0.041	80.7 (20.4 – 177)	12.1
T2_24	52.369	129.046	0.179	0.023			-	
T2_25	63.662	130.309	0.231	0.005	0.21		90.8 (22.9 – 145)	
T2_26	19.724	97.574	0.142	0.002	0.10		-	
T2_27	21.388	95.084	0.089				-	
T2_28	-14.779	4.953	0.324	0.006	0.19		14.7 (4.7 – 28.7)	
T2_30	-48.723	4.457	0.234	0.010	0.21		97.5 (16.5 – 229)	68.46
T2_35	21.818	18.700	0.149	0.005				
T2_36	-51.922	-25.035	0.244	0.006				

T2_37	58.632	-30.241	0.112	0.008				
T2_41	-54.009	150.654	0.119	0.010				
T2_42	35.523	147.644	0.061	0.002				
T2_44	65.124	-78.536	0.231		0.19		218 (81 – 323.3)	42
T2_45	50.118	-124.308	0.088	0.006	0.06		75.4 (32.3 – 208)	19.405
T2_46	-1.697	10.924	0.192	0.007	0.10		19.5 (10.3 – 42.4)	4.821
T2_47	-3.516	10.063	0.208	0.015	0.12	0.009	18.46 (11.6 – 46.5)	5.66

REFERENCES

- Ammannito, E. et al. (2016). Distribution of phyllosilicates on the surface of Ceres, *Science*, 353(6303), doi:10.1126/science.aaf4279.
- Anderson, D. M., and P. Hoekstra (1965). Crystallization of Clay-Adsorbed Water, *Science*, 149(3681), 318–319.
- Arenson, L. U., M. M. Johansen, and S. M. Springman (2004). Effects of Volumetric Ice Content and Strain Rate on Shear Strength under Triaxial Conditions for Frozen Soil Samples, *Permagrost and Periglacial Processes*, 15, 261–271, doi:10.1002/ppp.498.
- Barber, D. J. (1981). Matrix phyllosilicates and associated minerals in C2M carbonaceous chondrites, *Geochimica Cosmochimica Acta*, 45(6), 945–970.
- Bass, M. N. (1971). Montmorillonite and serpentine in Orgueil meteorite, *Geochimica Cosmochimica Acta*, 35(2), 139–147.
- Beeman, M., W. B. Durham, and S. H. Kirby (1988). Friction of ice, *Journal of Geophysical Research*, 93(B7), 7625, doi:10.1029/JB093iB07p07625.
- Behnsen, J., and D. R. Faulkner (2012). The effect of mineralogy and effective normal stress on frictional strength of sheet silicates, *Journal of Structural Geology*, 42, 49–61, doi:10.1016/j.jsg.2012.06.015.
- Bland, M. T. et al. (2016). Composition and structure of the shallow subsurface of Ceres revealed by crater morphology, *Nature Geoscience*, 9(7), 538–542, doi:10.1038/ngeo2743.
- Bland, P. A., and B. J. Travis (2017). Giant convecting mud balls of the early solar

- system, *Science advances*, 3(7), e1602514.
- De Blasio, F. V. (2011a). *Introduction to the Physics of Landslides*, Springer Netherlands, Dordrecht.
- De Blasio, F. V. (2011b). Landslides in Valles Marineris (Mars): A possible role of basal lubrication by sub-surface ice, *Planetary and Space Science*, 59(13), 1384–1392, doi:10.1016/j.pss.2011.04.015.
- De Blasio, F. V. (2014). Geomorphology Friction and dynamics of rock avalanches travelling on glaciers, *Geomorphology*, 213, 88–98, doi:10.1016/j.geomorph.2014.01.001.
- Buczkowski, D. L. et al. (2016). The geomorphology of Ceres, *Science*, 353(6303), doi:10.1126/science.aaf4332.
- Campbell, C. S. (1989). Self-Lubrication for Long Runout Landslides, *Journal of Geology*, 97(6), 653-665.
- Castillo-Rogez, J., and E. D. Young (2017). Origin and evolution of volatile-rich asteroids, *Planetesimals: Early Differentiation and Consequences for Planets*.
- Castillo-Rogez, J. C. et al. (2016). Loss of Ceres' Icy Shell from Impacts: Assessment and Implications, *Lunar and Planetary Science Conference*, #3012.
- Christ, M., and Y. Kim (2009). Experimental Study on the Physical-Mechanical Properties of Frozen Silt, *KSCE Journal of Civil Engineering*, 13(5), 317–324, doi:10.1007/s12205-009-0317-z.
- Chuang, F. C., and R. Greeley (2000). Large mass movements on Callisto, *Journal of Geophysical Research: Planets*, 105(E8), 20227–20244, doi:10.1029/2000JE001249.
- Cleary, P. W., and C. S. Campbell (1993). Self-lubrication for Long Runout Landslides: Examination by computer simulation, *Journal of Geophysical Research*, 98(B12), 21911–21924, doi:10.1029/93jb02380.
- Combe, J. et al. (2016). Detection of local H₂O exposed at the surface of Ceres, *Science*, 353(6303), doi:10.1126/science.aaf3010.
- Combe, J. et al. (2018). The surface composition of Ceres' Ezinu quadrangle analyzed by the Dawn mission, *Icarus*, in press, doi:10.1016/j.icarus.2017.12.039.
- Combe, J.-P. et al. (2017). Exposed H₂O-rich areas on Ceres detected by Dawn, *Lunar and Planetary Science Conference*, #2568.
- Cruden, D. M., and B. K. Lucchitta (1980). A large landslide on Mars: Discussion and

- reply, *Geological Society of America Bulliten*, 91(1), 63–64.
- Dade, W. B., and H. E. Huppert (1998). Long-runout rockfalls, *Geology*, 26(9), 803–806.
- Davies, T. R. H. (1982). Spreading of rock avalanche debris by mechanical fluidization, *Rock Mechanics*, 15, 9–24, doi:10.1007/BF01239474.
- Dodson-Robinson, S. E., K. Willacy, P. Bodenheimer, N. J. Turner, and C. A. Beichman (2009). Ice lines, planetesimal composition and solid surface density in the solar nebula, *Icarus*, 200(2), 672–693, doi:10.1016/j.icarus.2008.11.023.
- Dyl, K. A., et al., (2012). Early Solar System hydrothermal activity in chondritic asteroids on 1 – 10-year timescales, *Proceedings of the National Academy of Sciences*, 109(45), 18306–18311, doi:10.1073/pnas.1207475109.
- Erismann, T. H., and G. Abele (2013). *Dynamics of Rockslides and Rockfalls*, Springer Science & Business Media.
- Evans, S. G., G. S. Mugnozza, A. Strom, and R. L. Hermanns (2002). *Landslides from Massive Rock Slope Failure*, (Vol 49), Springer Science & Business Media.
- Fahnestock, R. K. (1978). Little Tahoma Peak Rockfalls and Avalanches, Mount Rainier, Washington, U.S.A., in *Developments in Geotechnical Engineering*, Vol, 14, Elsevier, pp. 181–196.
- Formisano, M., et al., (2017). Thermal stability of water ice on Ceres' surface: The Juling case, *Lunar and Planetary Science Conference*, #1976.
- Fu, R. R. et al. (2017). The interior structure of Ceres as revealed by surface topography, *Earth and Planetary Science Letters*, 476, 153–164, doi:10.1016/j.epsl.2017.07.053.
- Goguel, J. (1978). Scale-Dependent Rockslide Mechanisms, with Emphasis on the Role of Pore Fluid Vaporization-Chapter 20, in *Developments in Geotechnical Engineering*, edited by B. Voight, pp. 693–706, Elsevier, Amsterdam.
- Goodman, R. E. (1980). *Introduction to Rock Mechanics*, 1st ed., John Wiley & Sons, New York, NY.
- Graham, J., and V. C. S. Au (1985). Effects of freeze–thaw and softening on a natural clay at low stresses, *Canadian Geotechnical Journal*, 22(1), 69–78.
- Guo, D., M. Hamada, C. He, Y. Wang, and Y. Zou (2014). An empirical model for landslide travel distance prediction in Wenchuan earthquake area, *Landslides*, 11(2), 281–291, doi:10.1007/s10346-013-0444-y.
- Hayashi, C. (1981). Structure of the solar nebula, growth and decay of magnetic

- fields and effects of magnetic and turbulent viscosities on the nebula, *Progress of Theoretical Physics Supplement*, 70, 35–53, doi:10.1143/PTPS.70.35.
- Hayne, P. O., and O. Aharonson (2015). Thermal stability of ice on Ceres with rough topography, *Journal of Geophysical Research: Planets*, 120(9), 1567–1584, doi:10.1002/2015JE004887.
- Heim, A. (1932). *Bergsturz und menschenleben*, No. 20., Fretz & Wasmuth.
- Hsü, K. J. (1975). Catastrophic Debris Streams (Sturzstroms) Generated by Rockfalls, *Geological Society of America Bulletin*, 86(1), 129–140.
- Iverson, R. M. (1997). The Physics of Debris Flows, *Reviews of geophysics*, 35(3), 245–296.
- Iverson, R. M. et al. (2015). Landslide mobility and hazards: Implications of the 2014 Oso disaster, *Earth and Planetary Science Letters*, 412, 197–208, doi:10.1016/j.epsl.2014.12.020.
- Johnson, V., and F. P. Fanale (1973). Optical Properties of Carbonaceous Chondrites and Their Relationship to Asteroids, *Journal of Geophysical Research*, 78(35), 8507–8518.
- Kaufhold, S., M. Hein, R. Dohrmann, and K. Ufer (2012). Vibrational Spectroscopy Quantification of the mineralogical composition of clays using FTIR spectroscopy, *Vibrational Spectroscopy*, 59, 29–39, doi:10.1016/j.vibspec.2011.12.012.
- Kennedy, F. E., E. M. Schulson, and D. E. Jones (2000). The friction of ice on ice at low sliding velocities, *Philosophical Magazine A*, 80(5), 1093–1110, doi:10.1080/01418610008212103.
- Kent, P. (1966). The transport mechanism in catastrophic rock falls, *Journal of Geology*, 74(1), 79–83.
- Kozłowski, T., and E. Nartowska (2013). Unfrozen water content in representative Bentonites of Different Origin Subjected to Cyclic Freezing and Thawing, *Vadose Zone*, 12(1), doi:10.2136/vzj2012.0057.
- Küppers, M. et al. (2014). Localized sources of water vapour on the dwarf planet (1) Ceres, *Nature*, 505(7484), 525–527, doi:10.1038/nature12918.
- Landis, M. E. et al. (2017). Conditions for sublimating water ice to supply Ceres' exosphere, *Journal of Geophysical Research: Planets*, 122(10), 1984–1995, doi:10.1002/2017JE005335.
- Larsen, I. J., D. R. Montgomery, and O. Korup (2010). Landslide erosion controlled by

- hillslope material, *Nature Geoscience*, 3(4), 247–251, doi:10.1038/ngeo776.
- Lebofsky, L. A., M. A. Feierberg, A. T. Tokunaga, H. P. Larson, and J. R. Johnson (1981). The 1.7- to 4.2- μm spectrum of asteroid 1 Ceres : Evidence for structural water in clay minerals, *Icarus*, 48(3), 453-459.
- Legros, F. (2002). The Mobility of Long-Runout Landslides, *Engineering Geology*, 63(3–4), 301–331, doi:10.1016/S0013-7952(01)00090-4.
- Li, H., Y. Zhu, J. Zhang, and C. Lin (2004). Effects of Temperature, Strain Rate and Dry Density on Compressive Strength of Saturated Frozen Clay, *Cold Regions Science and Technology*, 39(1), 39–45, doi:10.1016/j.coldregions.2004.01.001.
- Lucchitta, B. K. (1979). Landslides in Valles Marineris, Mars, *Journal of Geophysical Research*, 84(9), 8097, doi:10.1029/JB084iB14p08097.
- Martin, R. G., and M. Livio (2013). On the Evolution of the Snow Line in Protoplanetary Discs - II. Analytic Approximations, *Monthly Notices of the Royal Astronomical Society*, 434(1), 633–638, doi:10.1093/mnras/stt1051.
- McCord, T. B., and C. Sotin (2005). Ceres: Evolution and Current State, *Journal of Geophysical Research*, 110(E5), 1–14, doi:10.1029/2004JE002244.
- McEwen, A. S. (1989). Mobility of Large Rock Avalanches: Evidence from Valles Marineris, Mars, *Geology*, 17(12), 1111–1114, doi:10.1130/0091-7613(1989)017<1111:MOLRAE>2.3.CO.
- McEwen, A. S., and M. C. Malin (1989). Dynamics of Mount St. Helens' 1980 Pyroclastic Flows, Rockslide Avalanche, Lahars, and Blast, *Journal of Volcanology and Geothermal Research*, 37(3-4), 205.
- Melosh, H. J. (1979). Acoustic Fluidization - A New Geologic Process?, *Journal of Geophysical Research*, 84(9), 7513–7520, doi:10.1029/JB084iB13p07513.
- Milliken, R. E., and A. S. Rivkin (2009). Brucite and Carbonate Assemblages from Altered Olivine-rich Materials on Ceres, *Nature Geoscience*, 2(4), 258–261, doi:10.1038/ngeo478.
- Mills, A. (2008). The Coefficient of Friction, Particularly of Ice, *Physics Education*, 43(4), 392.
- Morrow, C., B. Radney, and J. Byerlee (1992). Frictional Strength and the Effective Pressure Law of Montmorillonite and Illite Clays, *International Geophysics*, 51(C), 69–88, doi:10.1016/S0074-6142(08)62815-6.
- Othman, M. A., and C. H. Benson (1993). Effect of Freeze–Thaw on the Hydraulic Conductivity and Morphology of Compacted Clay, *Canadian Geotechnical*

Journal, 30(2), 236–246.

- Pardini, G., G. V. Guidi, R. Pini, D. Regiirs, and F. Gallart (1996). Structure and Porosity of Smectitic Mudrocks as Affected by Experimental Wetting-drying Cycles and Freezing-thawing Cycles, *Catena*, 27(3-4).
- Park, R., et al., (2015). Physical Properties of Ceres from the Dawn Mission, in *American Astronomical Society, DPS meeting #47*.
- Park, R. S. et al. (2016). A Partially Differentiated Interior for (1) Ceres Deduced from its Gravity Field and Shape, *Nature*, 537(7621), 515–517, doi:10.1038/nature18955.
- Platz, T., et al., (2016). Surface water-ice deposits in the northern shadowed regions of Ceres, *Nature Astronomy*, 1, 0007, doi:10.1038/s41550-016-0007.
- Plaut, J. J., et al., (2009). Radar evidence for ice in lobate debris aprons in the mid-northern latitudes of Mars, *Geophysical Research Letters*, 36(2), 5–8, doi:10.1029/2008GL036379.
- Prettyman, T. H. et al. (2016). Elemental composition of Ceres by Dawn’s Gamma Ray and Neutron Detector., *Lunar and Planetary Science Conference*, #2228.
- Prettyman, T. H. et al. (2017). Extensive water ice within Ceres? aqueously altered regolith: Evidence from nuclear spectroscopy, *Science*, 355(6320), 55–59, doi:10.1126/science.aah6765.
- Preusker, F., et al., (2016). Dawn at Ceres - Shape Model and Rotational State, *Lunar and Planetary Science Conference*, #1954.
- Quantin, C., P. Allemand, and C. Delacourt (2004). Morphology and geometry of Valles Marineris landslides, *Planetary and Space Science*, 52(11), 1011–1022, doi:10.1016/j.pss.2004.07.016.
- Raponi, A. et al. (2017). Water ice on Ceres’ surface as seen by Dawn-VIR: Properties retrieval by means of spectral modeling, *Lunar and Planetary Science Conference*, #2007.
- Raymond, C. A. et al. (2015). Interior Evolution of Ceres and Vesta Revealed by Dawn, in *American Geophysical Union, Fall Meeting*.
- Rivkin, A. S., E. L. Volquardsen, and B. E. Clark (2006). The surface composition of Ceres: Discovery of carbonates and iron-rich clays, *Icarus*, 185(2), 563–567, doi:10.1016/j.icarus.2006.08.022.
- Rubin, A. E. (2012). Collisional facilitation of aqueous alteration of CM and CV carbonaceous chondrites, *Geochimica et Cosmochimica Acta*, 90, 181–194,

doi:10.1016/j.gca.2012.05.016.

- Russell, C. T., and C. A. Raymond (2011). The Dawn Mission to Vesta and Ceres, *Space Science Reviews*, 163(1–4), 3–23, doi:10.1007/s11214-011-9836-2.
- Russell, C. T., et al., (2015). First Results of the Exploration of Ceres by Dawn, *IAU General Assembly 22*, p. 21738.
- Saffer, D. M., K. M. Frye, C. Marone, and K. Mair (2001). Laboratory results indicating complex and potentially unstable frictional behavior of smectite clay, *Geophysical Research Letters*, 28(12), 2297–2300, doi:10.1029/2001GL012869.
- De Sanctis, M. C. et al. (2015). Ammoniated phyllosilicates with a likely outer Solar System origin on (1) Ceres, *Nature*, 528(7581), 241–244, doi:10.1038/nature16172.
- De Sanctis, M. C. et al. (2016). One Year of Observations of Dawn at Ceres: Composition as seen by VIR, *EGU General Assembly*.
- Schenk, P., et al., (2015). Impact Craters on Ceres : Evidence for Water-Ice Mantle?, *EPSC Abstracts*, vol. 10, pp. 4–5.
- Schmidt, B. E. et al. (2017). Geomorphological Evidence for Ground Ice on Dwarf Planet Ceres, *Nature Geoscience*, 10(5), 338-343, doi:10.1038/ngeo2936.
- Schorghofer, N. (2016). Predictions of depth-to-ice on asteroids based on an asynchronous model of temperature, impact stirring, and ice loss, *Icarus*, 276, 88–95, doi:10.1016/j.icarus.2016.04.037.
- Schulson, E. M., and A. L. Fortt (2012). Friction of ice on ice, *Journal of Geophysical Research: Solid Earth*, 117(12), 1–18, doi:10.1029/2012JB009219.
- Shaller, P. J., and A. Smith-Shaller (1996). Review of proposed mechanisms for sturzstroms (long-runout landslides), in *Sturzstroms and Detachment Faults*, 185–202.
- Shreve, R. L. (1966). Sherman Landslide, Alaska, *Science*, 154(3757), 1639–1643, doi:10.1126/science.154.3757.1639.
- Shreve, R. L. (1968a). Leakage and fluidization in air-layer lubricated avalanches, *Geological Society of America Bulletin*, 79(5), 653–658..
- Shreve, R. L. (1968b). The Blackhawk Landslide, *Geological Society of America*, 108, 1–48.
- Sierks, H. et al. (2011). The Dawn Framing Camera, *Space Science Review*, 163(1–4), 263–327, doi:10.1007/s11214-011-9745-4.

- Singer, K. N., W. B. McKinnon, P. M. Schenk, and J. M. Moore (2012). Massive ice avalanches on Iapetus mobilized by friction reduction during flash heating, *Nature Geoscience*, 5(8), 574–578, doi:10.1038/ngeo1526.
- Stack, K. M., and R. E. Milliken (2015). Modeling near-infrared reflectance spectra of clay and sulfate mixtures and implications for Mars, *Icarus*, 250, 332–356, doi:10.1016/j.icarus.2014.12.009.
- Straub, S. (1996). Self-organization in the rapid flow of granular material: Evidence for a major flow mechanism, *Geologische Rundschau*, 85(1), 85–91, doi:10.1007/s005310050055.
- Straub, S. (1997). Predictability of long runout landslide motion: implications from granular flow mechanics, *Geologische Rundschau*, 86, 415–425, doi:10.1007/s005310050150.
- Svensson, P. D., and S. Hansen (2010). Freezing and thawing of montmorillonite - A time-resolved synchrotron X-ray diffraction study, *Applied Clay Science*, 49(3), 127–134, doi:10.1016/j.clay.2010.04.015.
- Takarada, S., T. Ui, and Y. Yamamoto (1999). Depositional features and transportation mechanism of valley-filling Iwasegawa and Kaida debris avalanches, Japan, *Bulletin of Volcanology*, 60(7), 508–522, doi:10.1007/s004450050248.
- Tembe, S., D. A. Lockner, and T. F. Wong (2010). Effect of clay content and mineralogy on frictional sliding behavior of simulated gouges: Binary and ternary mixtures of quartz, illite, and montmorillonite, *Journal of Geophysical Research: Solid Earth*, 115(3), 1–22, doi:10.1029/2009JB006383.
- Thomas, Parker, McFadden, Russell, Stern, Sykes, and Young (2005). Differentiation of the asteroid Ceres as revealed by its shape, *Nature*, 437, 224, doi:10.1038/nature03938.
- Ting, B. J. M., A. M. Asce, R. T. Martin, C. C. Ladd, and F. Asce (1984). Mechanisms of strength for frozen sand, *Journal of Geotechnical Engineering*, 109(10), 1286–1302.
- Tomeoka, K., and P. R. Buseck (1982). Intergrown mica and montmorillonite in the Allende carbonaceous chondrite, *Nature*, 299(5881), 326.
- Vardoulakis, I. (2000). Catastrophic landslides due to frictional heating of the failure plane, *Mechanics of Cohesive-Frictional Material*, 5(6), 443–467.
- Van Vliet-Lanoe, B., and A. Dupas (1991). Development of soil fabric by freeze/thaw cycles—its effect on frost heave, in *7th International Symposium on Ground Freezing*. Rotterdam, pp. 189–195.

- Voight, B., and J. Sousa (1994). Lessons from Ontake-san: A comparative analysis of debris avalanche dynamics, *Engineering Geology*, 38(3-4), 261-297, doi:10.1016/0013-7952(94)90042-6.
- Voight, B., R. J. Janda, H. Glicken, and P. M. Douglass (1983). Nature and mechanics of the Mount St Helens rockslide-avalanche of 18 May 1980, *Géotechnique*, 35(3), 357-368, doi:10.1680/geot.1985.35.3.357.
- Watkins, J. A., B. L. Ehlmann, and A. Yin (2015). Long-runout landslides and the long-lasting effects of early water activity on Mars, *Geology*, 43(2), 107-110, doi:10.1130/G36215.1.
- Yuanlin, Z., and D. L. Carbee (1984). Uniaxial Compressive Strength of Frozen Silt Under Constant Deformation Rates, *Cold Regions Science and Technology*, 9, 3-15.
- Zolotov, M. (2016). Salty Ceres, *Nature Geoscience*, 9, 476-477, doi:10.1038/ngeo2756.